Petroleum Science 20 (2023) 2664–2682

Contents lists available at ScienceDirect

Petroleum Science

journal homepage: www.keaipublishing.com/en/journals/petroleum-science

Original Paper

Quantitative characterization of vertical zonation of Mesozoic granite weathering reservoirs in the coastal area of eastern Fujian Province, China

Jing-Song Hu [a, b], Yi-Ming Jiang [c], Hua-Feng Tang [a, b, *], Wen-Rui Ma [c], Peng Tao [a, b], Ning-Yuan Sun [a, b]

[a] College of Earth Sciences, Jilin University, Changchun 130061, Jilin, China
[b] Key Laboratory of Mineral Resources Evaluation in Northeast Asia, Ministry of Natural Resources, Changchun 130061, Jilin, China
[c] CNOOC Shanghai Branch, Shanghai 200030, China

ARTICLE INFO

Article history:
Received 28 June 2022
Received in revised form
1 May 2023
Accepted 17 May 2023
Available online 18 May 2023

Edited by Jie Hao and Teng Zhu

Keywords:
Granite weathering crust
Vertical zonation of reservoir
Quantitative characterization
Eastern Fujian
Mesozoic granite

ABSTRACT

Weathering crust reservoirs have obvious vertical zonation, which is the focus of weathering crust reservoir research, but there is a lack of quantitative characterization indexes. To achieve the quantitative characterization of granite weathering crust reservoir and provide the basis for oil exploration of granite weathering crust buried hill reservoir, in this paper, the vertical zonation of granite weathering crust reservoir is quantitatively divided by testing and analyzing the uniaxial compressive strength (UCS), magnetic susceptibility (MS), permeability, and chemical index of alteration (CIA) of the Mesozoic granite weathering crust in the coastal area of eastern Fujian. The results show that the granite weathering crust reservoir can be divided into four zones vertically: a soil zone (SZ), weathered and dissolved zone (WDZ), fracture zone (FZ), and bedrock zone (BZ). A cataclastic area is developed in the FZ and BZ, in which structural fractures are well-developed, the fracture surface density is usually greater than 200 m/m^2, and the contribution to the fractures in the rock mass is up to about 50%, making this the sweet spot of the reservoir. In the SZ, the rocks are loose, and the pores are well-developed. The UCS is less than 10 MPa, and the average rate of change of the UCS ($\Delta\sigma$) is 0.90. The average permeability is 2823.00 mD, and the average rate of change of the permeability ($\Delta\kappa$) is 5.13. The average CIA is 74.9%. The average clay mineral content is 7%. The rocks in the WDZ have been significantly weathered by physical and chemical processes, and the weathering fractures and dissolution pores are well-developed. The average UCS is 18.2 MPa, and the average $\Delta\sigma$ is 0.70. The average permeability is 143.80 mD, and average $\Delta\kappa$ is 4.17. The average CIA is 65.3%. The average clay mineral content is 4%. Under the influence of tectonic movement and physical weathering, the rocks in the FZ have developed structural fractures and a few weathered fractures. The average UCS is 57.9 MPa, and the average $\Delta\sigma$ is 0.18. The average permeability is 5.50 mD, and the average $\Delta\kappa$ is 2.55. The average CIA is 61.6%. The average clay mineral content is 2%. In the BZ, the rocks are intact and hard. The average UCS is 69.9 MPa, and the average $\Delta\sigma$ is 0.13. The average permeability is 1.46 mD, and the average $\Delta\kappa$ is 1.43. The average CIA is 57.8%. The average clay mineral content is less than 1%. The multi-parameter combination of the UCS, $\Delta\sigma$, permeability, $\Delta\kappa$, CIA, and clay mineral content achieved good results in the division of the zones of the weathering crust. The UCS increases gradually from top to bottom, while $\Delta\sigma$, permeability, $\Delta\kappa$, CIA, and clay mineral content all decrease gradually. In addition, based on the petrophysical parameters of the rocks, including the density, resistivity, and acoustic velocity, a good division effect was also achieved, which can provide a basis for the vertical zonation of the granite buried-hill weathering crust reservoir.

1. Introduction

Since the 20th century, as a new field of oil and gas exploration,

* Corresponding author. College of Earth Sciences, Jilin University, Changchun 130061, Jilin, China.
E-mail address: tanghfhc@jlu.edu.cn (H.-F. Tang).

https://doi.org/10.1016/j.petsci.2023.05.011

many large-scale granite buried hills have been discovered around the world, including fractured granite buried hills in the La Paz and Mara oil fields in the Maracaibo Basin, Venezuela (Nelson et al., 2000; Koning, 2003); a fractured granite buried hill in the Bach Ho oilfield in the Cuu Long Basin, Vietnam (Cuong and Warren, 2009; Nguen and Isaev, 2017; Koning, 2020; Zhang et al., 2023); a Precambrian granite buried hill in the Sirte Basin, Libya (Williams, 1972; Gruenwald, 2001; Abdunaser, 2015; Eshanibli et al., 2020); the Kharir granite buried hill in the Late Jurassic faulted basin in Masilah, Yemen (Ellis et al., 1996; Harris et al., 2002); and a granite buried hill in the Suez Bay Basin, Egypt (Salah and Alsharhan, 1998; Alsharhan, 2003; El-Naby et al., 2009). Granite buried-hill reservoirs are weathering crust-type reservoirs with obvious vertical zonation. Many scholars have carried out research on the vertical zonation of granite buried-hill weathering crust.

At present, granite buried hills are divided into three or four zones. Some scholars classify them according to the degree of physical and chemical weathering, while others classify them according to the degree of tectonic movement. Based on the uniaxial compressive strength (UCS) and permeability, the granodiorite weathering crust in Bømlo Island in Norway has been divided into three zones: a bedrock zone, semi-weathered zone, and soil zone. The latter two have each been subdivided into two sub-zones (Riber et al., 2015, 2016, 2017, 2019; Alberto et al., 2021). The Archaean metamorphic granite buried hill in the BZ 19-6 structural belt has been divided into a strongly weathered zone, weathered fracture zone, inner fracture zone, and bedrock zone (Hou et al., 2019; Xu et al., 2019; Lu et al., 2020). Based on the analysis of cores, electric curves, and the physical properties of thin sections of the granite buried-hill reservoir in the Bohai Bay Basin, the buried hill has been divided into a weathered clay zone, weathered sandy zone, weathered fracture zone, and bedrock zone (Li et al., 2014; Wang et al., 2015; Hu et al., 2017; Ye et al., 2020a, 2020b, 2021; Zhu et al., 2020). The granite weathering crust in southern Vietnam has been divided into a bauxite zone, kaolin zone, and bedrock zone (Nguyen et al., 2004; Novikov et al., 2018). The weathering crust of the plutonic intrusive rocks in the Bongor Basin in southern Chad has been divided into a weathering leaching zone, fracture zone, semi-filled fracture zone, and dense zone (Dou et al., 2011, 2015, 2018; Yu et al., 2019). In the above zonation schemes, for both the three and four zone classifications, in terms of the physical properties of the reservoir, the weathered zone and fracture zone are generally superior to the soil zone and bedrock zone, making them more valuable for exploration and development.

However, the classification of the vertical zonation of granite weathering crusts is only qualitative or semi-quantitative at present, and there is very little quantitative and high-resolution geomechanical and petrophysical data. In this study, based on the above-described research, using a variety of physical and chemical parameters, including the uniaxial compressive strength (UCS), permeability, magnetic susceptibility (MS), and chemical index of alteration (CIA), the granite weathering crust in the eastern coastal area of Fujian Province, China, was analyzed, and a quantitative characterization scheme for the zonation of the granite weathering crust was established using more parameters to provide a basis for the zonation of granite buried hills in the East China Sea Basin and for oil and gas exploration in such areas.

2. Geologic setting

The eastern coastal area of Fujian is in the southeastern margin of Mainland China, the western margin of the Pacific Ocean, and the lithospheric thinning area around the Pacific Ocean. It is adjacent to the East China Sea and the Taiwan Strait to the east. It is part of the active continental margin belt of the Mesozoic-Cenozoic giant tectonic magmatic belt around the Pacific Ocean (Hu, 2014). Under the action of the subduction of the Kula Plate and the coastal boundary of the continental crust, NW, NE, NNE, and NNW trending fault networks have been generated in this area. Controlled by these faults, the distribution of the strata in Fujian developed a new trend from north to south and from west to east, creating a structural framework with east-west zoning and north-south blocking (Li et al., 2021; Xiao et al., 2021). The NE trending Nanping-Ninghua tectono-magmatic belt and the NE trending Zhenghe-Dapu fault zone intersect in the Nanping area, dividing Fujian into three terranes: northwest, southwest, and east Fujian (Xu et al., 2017). The Indosinian and Yanshanian magmatic activity produced the Early Yanshanian granite, Late Yanshanian granite, and Late Yanshanian volcanic rocks, which are currently exposed in the study area. The distribution scales of the Late Yanshanian volcanic rocks and granite are the largest (Liu et al., 2007; Zhao et al., 2019; Li et al., 2022). The subject of this study was the Late Yanshanian granite in the study area (Fig. 1).

3. Samples and methods

3.1. Samples

All of the samples were collected from the eastern coastal area of Fujian Province, and the specific information is presented in Table 1. A total of 85 samples were collected in this study, and 48 columnar samples were drilled. Thirty samples were selected for X-ray diffraction (XRD) analysis, 44 samples were selected for X-ray fluorescence (XRF) analysis, and 26 columnar samples were selected for porosity, permeability, density, acoustic velocity, and resistivity analyses.

3.2. Methods

Based on the auxiliary determination of the lithology via X-ray diffraction and major element analysis, the zonation of the granite weathering crust was characterized using multiple parameters, including the uniaxial compressive strength, permeability, and magnetic susceptibility of the rocks. These parameters were measured in the field using portable instruments. Because some of the samples of field outcrops were loose and in-situ data needed to be obtained, the use of portable instruments was a favorable method for obtaining data.

3.2.1. X-ray diffraction

The X-ray diffraction (XRD) analysis was conducted in the Key Laboratory of Mineral Resources Evaluation in Northeast Asia, Ministry of Natural Resources, Jilin University. According to the sample preparation requirements, 15 g of fresh and clean sample was washed with distilled water, air dried, finely crushed to 200 mesh using a primary crushing and ball mill, and analyzed after complete mixing. A DX-2007X-ray diffractometer (made in China) was used to conduct the analysis, and then, the peak value of the mineral content intensity was obtained. The mineral content was calculated according to the interpretation process.

3.2.2. Major elements

The major element analysis was conducted in the Key Laboratory of Mineral Resources Evaluation in Northeast Asia, Ministry of Natural Resources, Jilin University. Based on identification of the lithofacies characteristics, fresh rock samples were selected, washed with distilled water, dried, crushed to 200 mesh without polluting the samples, and analyzed using an X-ray fluorescence spectrometer (XRF), with a relative error of 1–3%.

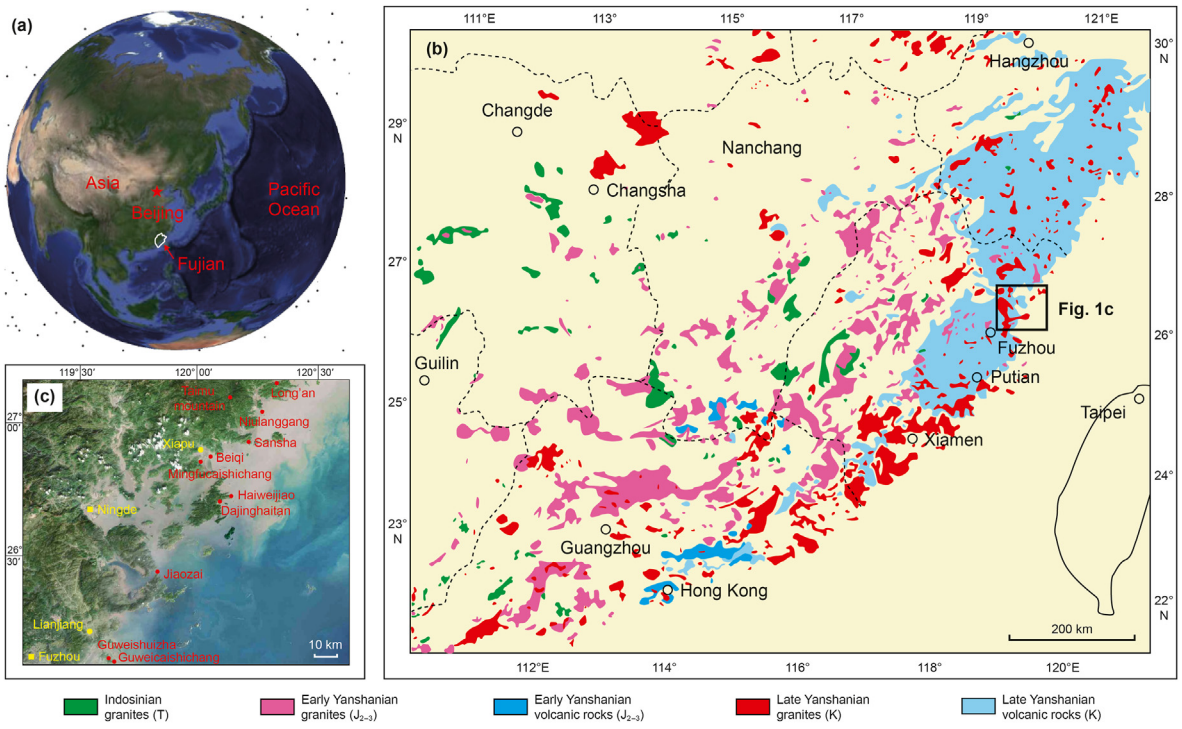

Fig. 1. Distribution and sampling locations of the Mesozoic igneous rocks in southeastern China (modified from Zhou and Li, 2000; Li et al., 2018; Niu et al., 2022). (a) Pilot map of Fujian Province. (b) Distribution of igneous rocks in the study area and adjacent areas. (c) Locations of field sampling.

Table 1
Characteristics and detailed information of outcrop samples in eastern coastal area of Fujian Province. SZ–soil zone, WDZ–weathered and dissolved zone, FZ–fracture zone, BZ–bedrock zone.

No.	Sampling location	GPS	Lithology	Zonation	Characterization of weathering	Sample name
1	Guweicaishichang, Lianjiang County	26°04′32.4″N, 119°38′46.4″E	Granite	SZ and WDZ	Physical and chemical weathering, the CIA ranges from 64% to 70%	GWCSC-1~ GWCSC-10
2	Guweishuizha, Lianjiang County	26°04′28.9″N, 119°38′57.1″E	Granite and granodiorite	FZ and BZ	Physical weathering, the CIA ranges from 62% to 66%	GWSZ-1~ GWSZ-7
3	Jiaozai, Lianjiang County	26°25′42.9″N, 119°50′16.0″E	Quartz monzonite	BZ	Physical weathering, the CIA ranges from 56% to 60%	JZ-1~JZ-4
4	Dajinghaitan, Xiapu County	26°42′28.5″N, 120°06′46.1″E	Granite	SZ, WDZ, and FZ	Physical and chemical weathering, the CIA ranges from 59% to 88%	XP-DJHT-1~XP-DJHT-11, XP-DJC-1~ XP-DJC-4
5	Haiweijiao, Xiapu County	26°43′37.3″N, 120°09′06.3″E	Granite	FZ and BZ	Physical weathering, the value of CIA is about 59%	XP-HWJ-1
6	Mingfu, Xiapu County	26°50′41.3″N, 120°01′04.6″E	Granite, granodiorite and quartz monzonite	WDZ and FZ	Physical and chemical weathering, the CIA ranges from 60% to 65%	XP-MF-1~ XP-MF-22
7	Beiqi, Xiapu County	26°52′40.2″N, 120°03′46.9″E	Granite	SZ, FZ	Physical and chemical weathering, the CIA ranges from 61% to 83%	XP-BQ-1~ XP-BQ-4
8	Sansha, Xiapu County	26°54′47.2″N, 120°13′30.9″E	Granite	SZ, WDZ, and FZ	Physical and chemical weathering, the CIA ranges from 60% to 68%	XP-SS-1~ XP-SS-5
9	Niulanggang, Fuding City	27°03′30.9″N, 120°16′47.9″E	Granite	WDZ and FZ	Physical and chemical weathering, the CIA ranges from 61% to 81%	FD-NLG-1~FD-NLG-7
10	Taimu mountain, Fuding City	27°07′33.8″N, 120°11′38.0″E	Granite	WDZ and FZ	Physical and chemical weathering, the CIA ranges from 57% to 71%	FD-TMS-1~FD-TMS-7
11	Long'an, Fuding City	27°10′40.4″N, 120°22′25.9″E	Granite	WDZ and FZ	Physical and chemical weathering, the CIA ranges from 64% to 65%	FD-LA-1~ FD-LA-3

3.2.3. Uniaxial compressive strength

The uniaxial compressive strength of the samples was measured using a digital Schmidt hammer instrument. The results were corrected based on international standards (ASTM d5873-00; EN 12 504-2; ASTM C 805-02) and were geomechanically characterized. The measurements were carried out directly on the selected representative outcrop. The test range of the instrument was 10–300 MPa (Aydin and Basu, 2005). During the measurements, the surface of the fresh rock was measured as often as possible. After the measurement points were selected according to the section length, each measurement point was measured and counted 6–8 times, with an interval of 1–2 cm in order to avoid deviations due to changes in the internal structure of the rock (such as compaction and microcracks) caused by the previous measurements. After the measurements, the geometric average value of the data, with an error of less than 10% for five measurements, was taken as the uniaxial compressive strength of the rock at this position. A total of 152 data points were measured and 835 uniaxial compressive strength data were obtained.

3.2.4. Permeability

The permeability was measured using a tiny perm^{-3} micro air permeability instrument, which was calibrated by New England Research (NER) using known standards. The instrument can measure the permeability of a rock within a small region (1–1.5 cm^3), with a measurement range of 10^{-2}–10^5 mD. During the measurement, the built-in compression container button is manually pressed. The instrument calculates the permeability according to the air flow output from the compression container and the calculation results are uploaded to the host. A total of 151 permeability data were obtained.

3.2.5. Magnetic susceptibility

An SM-30 portable magnetic susceptibility meter (ZH Company, Czech Republic) was used for the field measurements of the magnetic susceptibility, and its maximum measurement sensitivity was 1×10^{-7} SI. During the measurements, flat and fresh rock was selected as often as possible to ensure that the instrument stuck to the rock surface as much as possible without leaving gaps. Measurement points at different positions were selected according to the section length, and each point was measured 6–8 times. The data had an error of less than 1% for five replicate measurements, and the geometric average value was taken as the magnetic susceptibility value of the location. A total of 157 data points were measured and 830 susceptibility data were obtained.

3.2.6. Rate of change of the UCS ($\Delta\sigma$), rate of change of the permeability ($\Delta\kappa$), and chemical index of alteration

The $\Delta\kappa$, $\Delta\sigma$, and CIA were calculated as follows:

$$\Delta\kappa = \log[(\kappa_i - \kappa_{min})/\ \kappa_{min}], \quad (1)$$

$$\Delta\sigma = (\sigma_{max} - \sigma_i)/\ \sigma_{max}, \quad (2)$$

$$CIA = Al_2O_3/(Al_2O_3 + CaO^* + Na_2O + K_2O) \times 100\%, \quad (3)$$

where $\Delta\kappa$ is the rate of change of the permeability, κ_i is the permeability data for a certain measuring point, κ_{min} is the minimum value of all of the permeability values measured, which represents the permeability of the fresh rock, and $\kappa_i - \kappa_{min}$ is the difference between the permeability at the measuring point and the minimum value. The higher the value of $\kappa_i - \kappa_{min}$, the larger the value of $\Delta\kappa$, and the higher the degree of physical and chemical weathering of the measuring point. $\Delta\sigma$ is the rate of change of the UCS, σ_i is the UCS data for a certain measuring point, σ_{max} is the maximum value of all of the UCS measurements, which represents the UCS of the fresh rock, and $\sigma_{max} - \sigma_i$ is the difference between the UCS at the measuring point and the maximum value. The higher the value of $\sigma_{max} - \sigma_i$, the larger the value of $\Delta\sigma$, and the higher the degree of physical and chemical weathering of the measuring point. The mole fraction of each component is adopted in the CIA formula, and CaO* is the mole fraction of the CaO in the silicate. The formula:

$$CaO^* = CaO - (10/3 \times P_2O_5), \quad (4)$$

which is generally used for the calculation and correction of the CaO. In this study, the method proposed by McLennan (1993) was used to correct the CaO. During the chemical weathering of the upper crust, feldspar becomes the main parent rock mineral, and alkali metals such as Na, K, and Ca are lost in the form of ions and form clay minerals (e.g., kaolinite, montmorillonite, and illite). During this process, the mole fraction of Al_2O_3, i.e., the main component of the weathering products, changes with the chemical weathering intensity. Therefore, the CIA of granite can be used as an index to reflect the weathering degree of the source area (Shao and Yang, 2012; Xu and Shao, 2018).

3.2.7. Porosity and permeability

The analyses were conducted in the Central Lab of Applied Geophysics of Jilin University. A porosity and permeability under overpressure meter (AP-608) was used to test the porosity and permeability of helium (He) injection at 20 °C. The relevant procedures were carried out according to the standard of China's oil and gas industry for Conventional Core Analysis Method (SY/T 5336-2006).

3.2.8. Resistivity, acoustic velocity, and density

The analyses were conducted in the Central Lab of Applied Geophysics of Jilin University. A capillary pressure resistivity system (RCS-760) was used to test the resistivity. The maximum temperature could reach 150 °C, and the measurement frequency was 50–100 kHz. The experiment was carried out under full water conditions, the salinity of the simulated formation water was 51.23 g/L, and the specific gravity was 1.05. The vertical and horizontal acoustic velocities were measured using conventional testing equipment. The equipment included an Agilent MS07034B oscilloscope, Olympus 5077 PR ultrasonic pulse generator, and Olympus 1 MHz acoustic probe. The QL-600Z was used to test the density. The test adopted the principle of the Archimedes buoyancy method and followed ASTM C39 and other measurement standards. The vacuum saturation method and other operations were applied. The density of the sample was accurately converted to 1.000 g/cm^3 when the temperature of the water was 4 °C.

4. Petrological characteristics

According to the microscope observations of rock thin sections, granite, granodiorite, and quartz monzonite were identified at the sampling points in the study area. Granite was the main lithology, and the main diagenetic minerals included quartz, plagioclase, and alkali feldspar, as well as a small amount of dark minerals such as biotite. Under the influence of chemical dissolution, some of the biotite had been altered to chlorite, the main diagenetic minerals had also been subjected to different degrees of chemical dissolution, and some of the plagioclase and alkali feldspar had been altered to clay minerals such as kaolin (Fig. 2).

To further determine the lithology and mineral composition, the field samples were analyzed via XRD and XRF. According to the XRD results, quartz, plagioclase, and alkali feldspar were selected for projection. The quartz-alkali feldspar-plagioclase (QAP) ternary diagram revealed that the main diagenetic minerals in the samples were quartz, plagioclase, and alkali feldspar, as well as a small amount of dark minerals (mainly biotite and amphibole). Some of the rock samples also contained a small amount of clay minerals, such as chlorite, kaolinite, illite, and montmorillonite. Based on the microscopic thin section identification, it was determined that the lithologies at the field sampling points were mainly granite, granodiorite, and quartz monzonite (Fig. 3a). According to the major element analysis, the SiO_2 and $Na_2O + K_2O$ parameters were selected for mapping. The total alkali silica (TAS) diagram confirmed that the lithologies of the field samples were mainly granite, granodiorite, and quartz monzonite, which is consistent with the XRD and microscopic thin section identification results (Fig. 3b).

5. Vertical zonation and quantitative characterization of granite weathering crust

Some of the field outcrops exhibited good vertical zonation of the granite weathering crust. Based on the outcrop characteristics

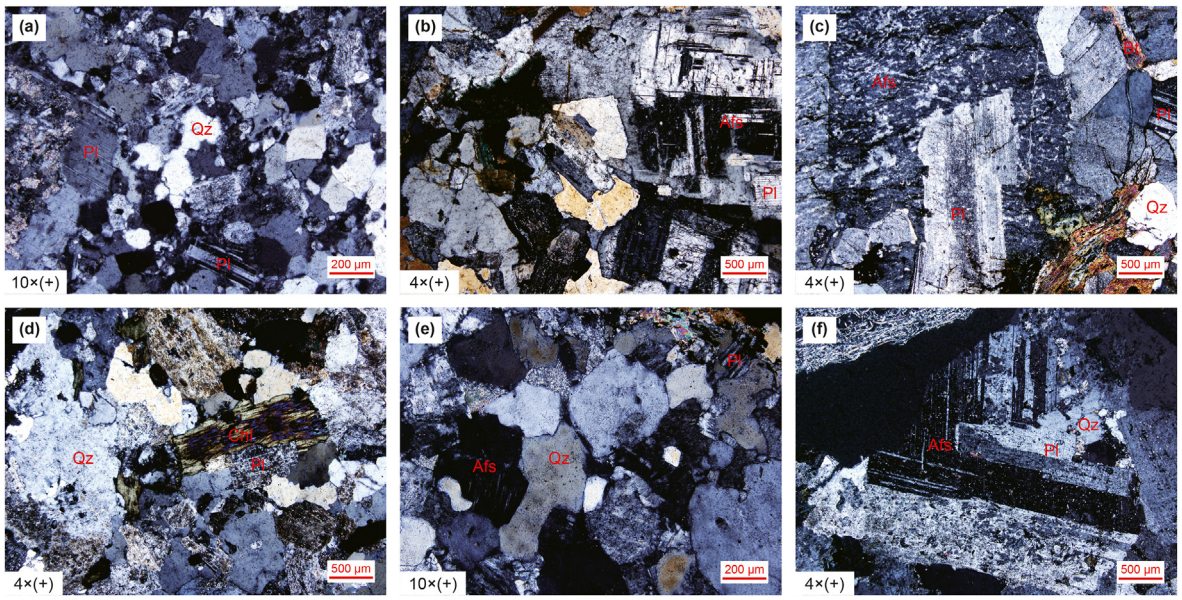

Fig. 2. Mesozoic rocks in the eastern coastal area of Fujian Province. (a) 26°04′28.9″N, 119°38′57.1″E, granodiorite. (b) 26°50′41.3″N, 120°01′04.6″E, granodiorite. (c) 27°10′40.4″N, 120°22′25.9″E, granite. (d) 26°52′40.2″N, 120°03′46.9″E, granite. (e) 26°54′48″N, 120°13′30.2″E, quartz monzonite. (f) 26°50′41.3″N, 120°01′02.1″E, quartz monzonite. Qz—quartz; Afs—alkali feldspar; Pl—plagioclase; Chl—chlorite; Bt—biotite.

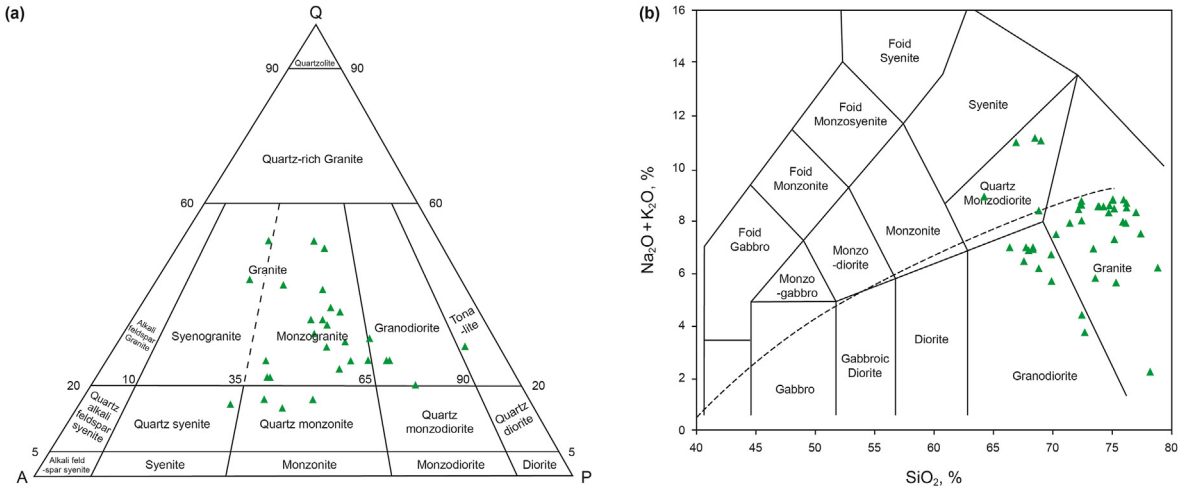

Fig. 3. (a) QAP diagram (after Streckeisen, 1976) and (b) TAS diagram for the Mesozoic granites in the eastern coastal area of Fujian Province.

and corresponding analysis results, the field outcrops were divided into zones. Based on the vertical zonation division scheme proposed by scholars such as Dou et al. (2015), Hou et al. (2019), Ye et al. (2020a), and Alberto et al. (2021), in this study, the vertical zonation of the Mesozoic granite weathering crust in the eastern coastal area of Fujian was conducted based on UCS, permeability, and CIA, and the weathering crust was divided into four zones vertically: a soil zone (SZ), weathered and dissolved zone (WDZ), fracture zone (FZ), and bedrock zone (BZ). The outcrops in the Guwei quarry and Guwei sluice were taken as examples to illustrate the classification scheme.

5.1. Soil zone

The soil zone is defined as the area where the rocks in the surface of the Earth's crust has been subjected to intense physical and chemical weathering to form sandy soil. It is located at the top of the weathering crust, generally has a small thickness and soft rocks, is mostly weathered into sandy soil, and can even be covered by vegetation. Dissolution pores and weathering fractures are developed. Taking the outcrop in Guwei quarry as an example, the characteristics of the soil zone and the various data for the rock are shown in Fig. 4. Because this zone has the strongest physical and chemical weathering, the UCS was lower than the test range of the instrument (< 10 MPa). The magnetic susceptibility was 1.60–1.73 ($4\pi \times 10^{-3}$ SI), with a geometric average of 1.65 ($4\pi \times 10^{-3}$ SI). The permeability was 2300.00–4150.00 mD, with a geometric average of 2900.00 mD. The CIA was 67.6–83.6%, with a geometric average of 71.3%.

5.2. Weathered and dissolved zone

The weathered and dissolved zone is defined as the area where the rocks in the surface of the Earth's crust have been subjected to

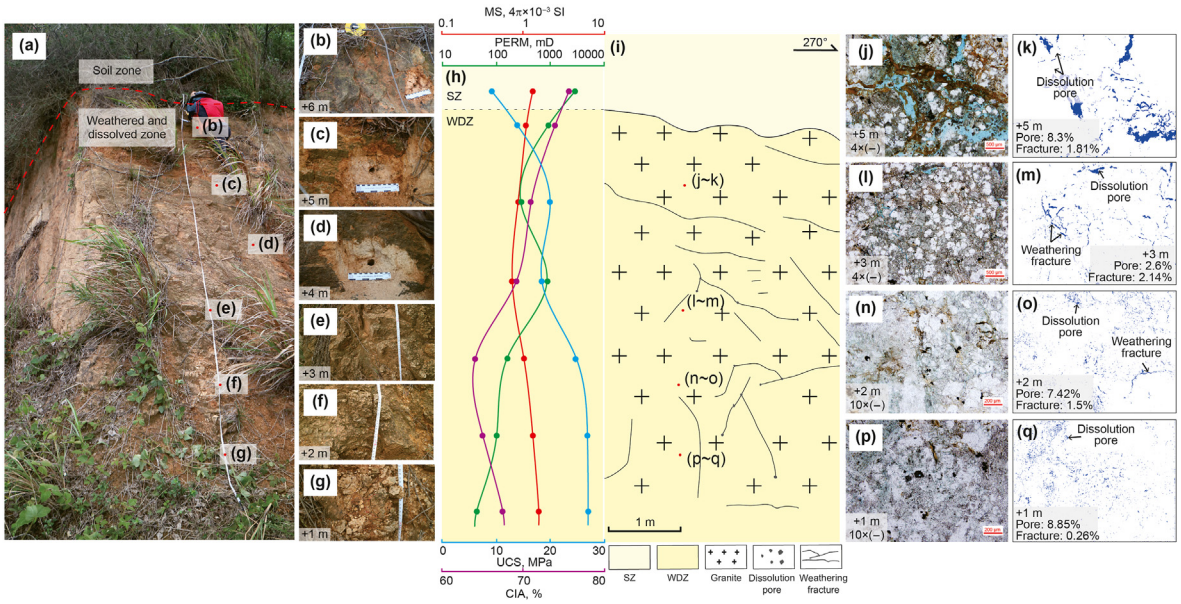

Fig. 4. Characteristics of the soil zone and weathered and dissolved zone of the Mesozoic granite weathering crust in Guwei quarry, Lianjiang County, Fujian Province. (a–g) Field outcrop and partial photos. (h) Physical and chemical parameters of the rocks. (i) Sketch of a field outcrop. (j–q) Images of cast thin sections and porosity and fracture quantification analysis. SZ–soil zone, WDZ–weathered and dissolved zone.

strong physical and chemical weathering and weathering fractures and dissolution pores have formed in the rocks. It is located under the soil zone. Taking the outcrop in Guwei quarry as an example, the characteristics of the weathered and dissolved zone and the various data for the rock are shown in Fig. 4. Due to the high degree of weathering, the UCS was lower than the test range of the instrument (< 10 MPa). The magnetic susceptibility was 0.90–1.83 ($4\pi \times 10^{-3}$ SI), with a geometric average of 1.34 ($4\pi \times 10^{-3}$ SI). The permeability was 64.00–943.00 mD, with a geometric average of 411.70 mD. The CIA was 64.1–74.1%, with a geometric average of 68.4%. There were cast thin sections of +1 m, +2 m, +3 m, and +5 m, and thin section porosity quantification analysis was conducted. The results revealed that the reservoir space was composed of dissolution pores and microfractures, and the thin section porosity was 4.74–10.11%. Among them, the dissolution pores were relatively well developed, accounting for 3.89–8.85%, with a geometric average of 7.12%; followed by the weathered microfractures, accounting for 0.26–1.81%, with a geometric average of 1.02% (Fig. 4j–q).

5.3. Fracture zone

The fracture zone is defined as the area where the rocks in the surface of the Earth's crust have been subjected to tectonic movement and physical weathering and structural and weathering fractures have formed in the rocks. It is located under the weathered and dissolved zone. According to the field observations, due to the different mineral compositions of the rocks, the rocks in the fracture zone had been subjected to different degrees of tectonic movement, and some areas were seriously cut by fractures, forming a cataclastic area. Some of the cataclastic areas had also been subjected to slight physical weathering, forming weathering fractures. The other parts of the fracture zone (i.e., everything except the cataclastic area) were defined as the non-cataclastic area. Taking the outcrop in the Guwei sluice as an example, the characteristics of the fracture zone and the various data for the rocks are shown in Fig. 5. The UCS was 67.9–71.3 MPa, with a geometric average of 69.3 MPa. The magnetic susceptibility was 1.51–11.52 ($4\pi \times 10^{-3}$ SI), with a geometric average of 3.97 ($4\pi \times 10^{-3}$ SI). The permeability was 0.08–0.28 mD, with a geometric average of 0.17 mD. The CIA was 62.4–66.2%, with a geometric average of 64.3%. In the 2.5–3.5 m area (vertically), due to the strong effect of the tectonic shear force, the rock had been seriously broken and many rhombus shaped blocks had developed. This was defined as the cataclastic area. The UCS in this area was 58.3 MPa, the permeability was 65.00 mD, the magnetic susceptibility was 3.40 ($4\pi \times 10^{-3}$ SI), and the CIA was 61.2%. Based on the casting thin sections, the reservoir space in this area was composed of structural fractures and dissolution pores, with a thin section porosity of 7.91%. The fractures were relatively well developed, accounting for a porosity of 6.54%, and were mainly structural fractures, but some of the fractures had been filled. The dissolution pores accounting for a porosity of about 1.37%.

5.4. Bedrock zone

The bedrock zone is defined as an area of solid rock that is more complete in the surface of the Earth's crust. It is located at the bottom of the weathering crust. The rock in this zone is almost unaffected by physical and chemical weathering, but some areas have been affected by tectonic movement, resulting in the formation of cataclastic areas and fractures. The other areas (i.e., everything except the cataclastic area) are defined as the non-cataclastic area, which is characterized by solid rocks and a lack of fractures. Taking the outcrop in the Guwei sluice as an example, the characteristics of the bedrock zone and the various data for the rock are shown in Fig. 5. The UCS was 78.3 MPa, the magnetic susceptibility was 8.71 ($4\pi \times 10^{-3}$ SI), the permeability was 0.06 mD, and the CIA was 59.3%.

5.5. Multi-parameter quantitative characterization of zonation of granite weathering crust

5.5.1. UCS

The UCS results are shown in Fig. 6. The UCS of the soil zone was very low, and the values were lower than the test range of the

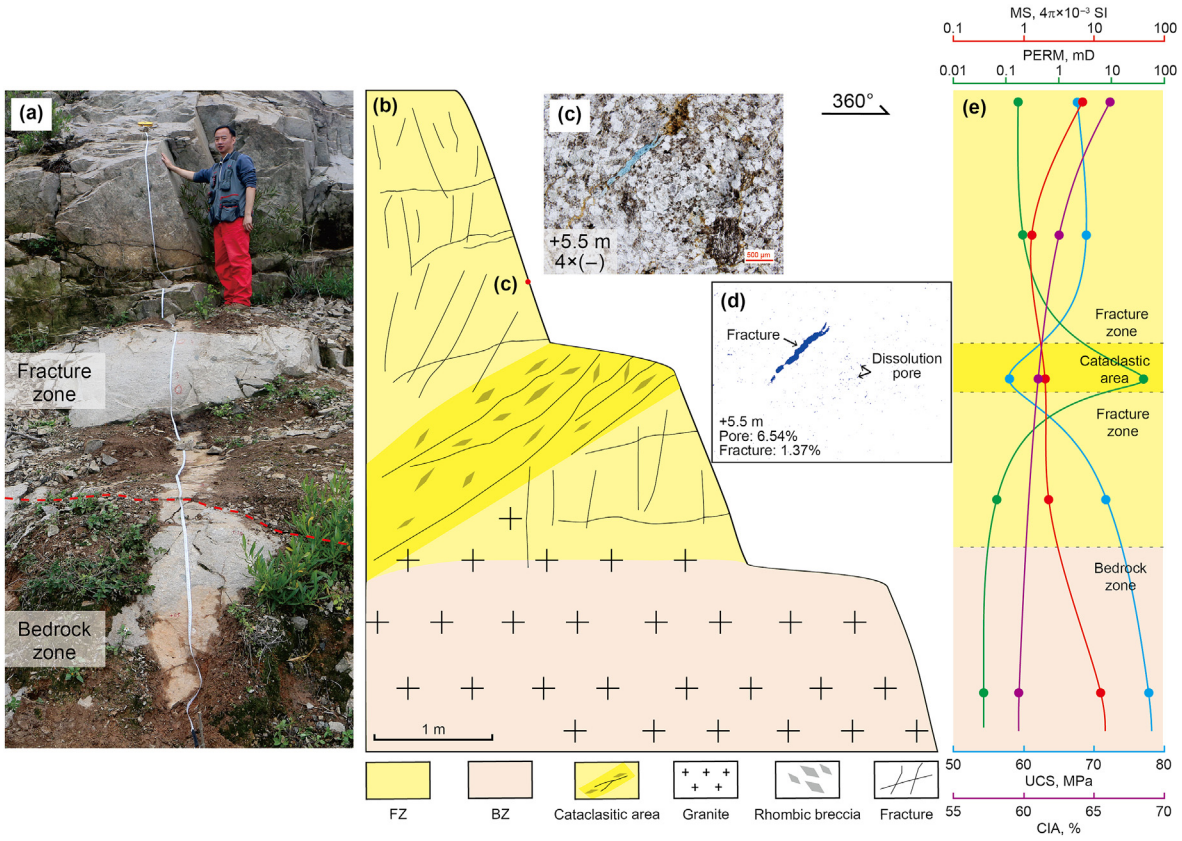

Fig. 5. Characteristics of the fracture zone and the bedrock zone of the Mesozoic granite weathering crust in the Guwei sluice, Lianjiang County, Fujian Province. (a) and (b) Field outcrop and sketch. (c) and (d) Image of cast thin section and porosity and fracture quantification analysis. (e) Physical and chemical parameters of the rocks. FZ–fracture zone, BZ–bedrock zone.

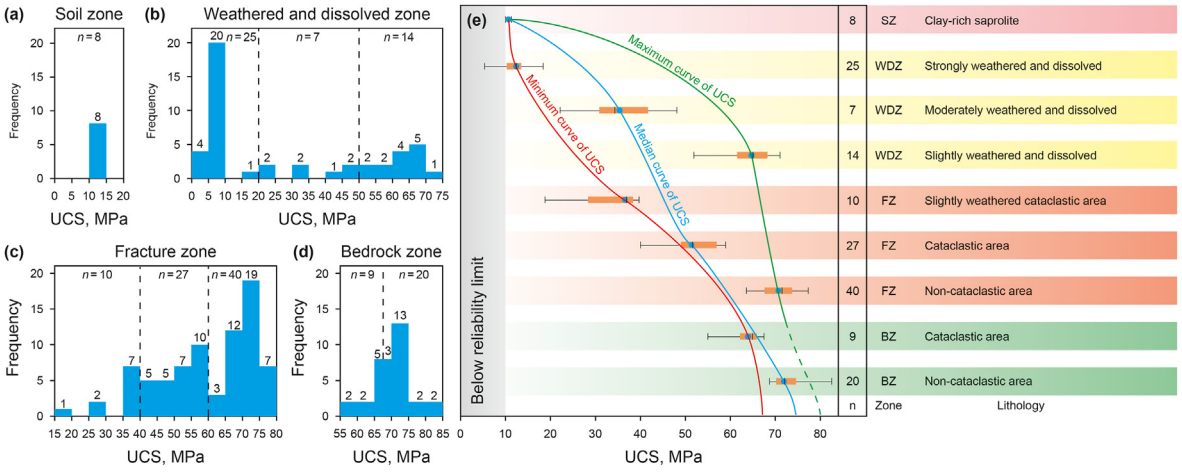

Fig. 6. Characteristics of the uniaxial compressive strength of the Mesozoic granite in the eastern coastal area of Fujian Province (MPa). (a) UCS distribution in the weathered and dissolved zone. (b) UCS distribution in the fracture zone. (c) UCS distribution in the bedrock zone. (d) Box diagram: The green circle represents the geometric mean of the effective data (data located in 1/4–3/4 of the entire dataset), and the vertical line represents the median of the entire dataset. N is the number of data in each group. The green, blue and red lines represent three possible trends in the field sections. The solid line is the measured data, and the dotted line is the predicted data. SZ–soil zone, WDZ–weathered and dissolved zone, FZ–fracture zone, BZ–bedrock zone.

instrument (< 10 MPa). The UCS data for the soil zone were obtained from Alberto et al. (2021) (Fig. 6a). The UCS of the weathered and dissolved zone was 10.0–70.8 MPa, with a geometric average of 18.2 MPa (Fig. 6b). Due to the different mineral compositions and contents, the physical and chemical weathering were heterogeneous, so the UCS of this zone was divided into three sections. The first section had been subjected to strong physical and chemical weathering, with UCS values of less than 10.0 MPa and a maximum of 18.0 MPa. The second section had been subjected to moderate physical and chemical weathering, with UCS values of 21.6–47.8 MPa. The third section had been subjected to slight physical and chemical weathering, or fresher rock was exposed as a

result of the peeling off of the weathered and dissolved rock surface (such as spherical weathered stone eggs), with UCS values of 51.8–70.8 MPa. The UCS of the fracture zone was 18.4–74.9 MPa, with a geometric average value of 57.9 MPa (Fig. 6c). Due to the different degrees of influence of the tectonic movement and physical weathering, the UCS of this zone was also divided into three sections. The first section was the part of the cataclastic area that had been affected by slight physical weathering. Structural and weathering fractures were developed, and the UCS values were lower (18.4–39.7 MPa). The second section was the part of the cataclastic area that had not been affected by physical weathering, with UCS values of 40.8–59.8 MPa. The third section was the non-cataclastic area, which had large UCS values of 63.2–78.3 MPa. The UCS of the bedrock zone was 55.1–83.5 MPa, with a geometric average value of 69.9 MPa (Fig. 6d). The bedrock zone also contained a cataclastic area, with UCS values of 55.1–67.5 MPa. The UCS values of the non-cataclastic area of the bedrock zone were 68.3–83.5 MPa. In conclusion, from top to bottom, the UCS of the section gradually increased (Fig. 6e).

5.5.2. Permeability

The permeability measurement results are shown in Fig. 7. The permeability of the rock in the soil zone was high, ranging from 1.44×10^3 to 1.12×10^4 mD (geometric average of 2.82×10^3 mD), because this zone had experienced the strongest weathering and had the loosest rocks (Fig. 7a). The permeability of the rocks in the weathered and dissolved zone was generally lower than that in the soil zone, with a geometric average of 1.44×10^2 mD (Fig. 7b). Similar to the UCS, the permeability of the weathered and dissolved zone was also divided into three sections. The permeabilities of the first, second, and third sections were 1.33×10^2–1.15×10^4 mD, 2.77×10^1–1.00×10^2 mD, and 5.00×10^{-2}–2.40×10^1 mD, respectively. The rock in the fracture zone had been affected by tectonic movement and physical weathering. The permeability was 2.00×10^{-2}–1.30×10^3 mD, with a geometric average of 5.50 mD (Fig. 7c). The permeability of the rock in the cataclastic area that had been subjected to slight physical weathering was 2.58×10^2–1.30×10^3 mD, while that of the rock in the cataclastic area without physical weathering was 1.08×10^1–1.87×10^2 mD, and that of rock in the non-cataclastic area was 2.00×10^{-2}–9.10 mD. The permeability of the bedrock zone was 2.00×10^{-2}–6.13×10^1 mD, with a geometric average of 1.46 mD (Fig. 7d). The permeability of the rock in the cataclastic area of the bedrock zone was 4.80–6.13×10^1 mD, and the permeability in the non-cataclastic area was 2.00×10^{-2}–3.90 mD. In conclusion, from top to bottom, the permeability of the weathering crust gradually decreased (Fig. 7e).

5.5.3. Magnetic susceptibility

The results of the magnetic susceptibility measurements are shown in Fig. 8. The magnetic susceptibility of the rocks in the soil zone was 1.05–3.21 ($4\pi \times 10^{-3}$ SI), with a geometric average of 2.44 ($4\pi \times 10^{-3}$ SI) (Fig. 8a). The magnetic susceptibility of the rocks in the weathered and dissolved zone was heterogeneous, ranging from 0.08 to 14.26 ($4\pi \times 10^{-3}$ SI), with a geometric average of 2.01 ($4\pi \times 10^{-3}$ SI) (Fig. 8b). The magnetic susceptibility of the rocks in the fracture zone was 0.05–11.56 ($4\pi \times 10^{-3}$ SI) (Fig. 8c). The magnetic susceptibility of the rocks in the bedrock zone was 0.35–6.51 ($4\pi \times 10^{-3}$ SI), with a geometric average of 3.55 ($4\pi \times 10^{-3}$ SI) (Fig. 8d). There was no obvious regularity to the variations in the magnetic susceptibility from top to bottom in the weathering crust (Fig. 8e).

5.5.4. $\Delta\kappa$, $\Delta\sigma$, CIA, and clay mineral content

In addition to the good correlations between the UCS and permeability and the zonation, the distribution ranges of the UCS and permeability of each zone were large, and the zonation could not be described well by a single parameter. Therefore, in this study, the parameters were compared by calculating $\Delta\sigma$, $\Delta\kappa$, and CIA. The CIA data are presented in Table 2. The results show that the combination of $\Delta\sigma$, $\Delta\kappa$, and CIA has a good effect in terms of the quantitative characterization of the zonation. $\Delta\kappa$ in the soil zone ranged from 4.00 to 7.00, with a geometric average of 5.13. $\Delta\sigma$ ranged from 0.75 to 1.00, with a geometric average of 0.90. The CIA was 67.0–85.0%, with a geometric average of 74.9% (Fig. 9). The clay mineral content was 5–8%, with a geometric average of 7% (Table 3). $\Delta\kappa$ in the weathered and dissolved zone ranged from 2.50 to 5.50, with a geometric average of 4.17. $\Delta\sigma$ ranged from 0.45 to 0.90, with a geometric average of 0.70. The CIA was 62.0–75.0%, with a geometric average of 65.3% (Fig. 9). The clay mineral content

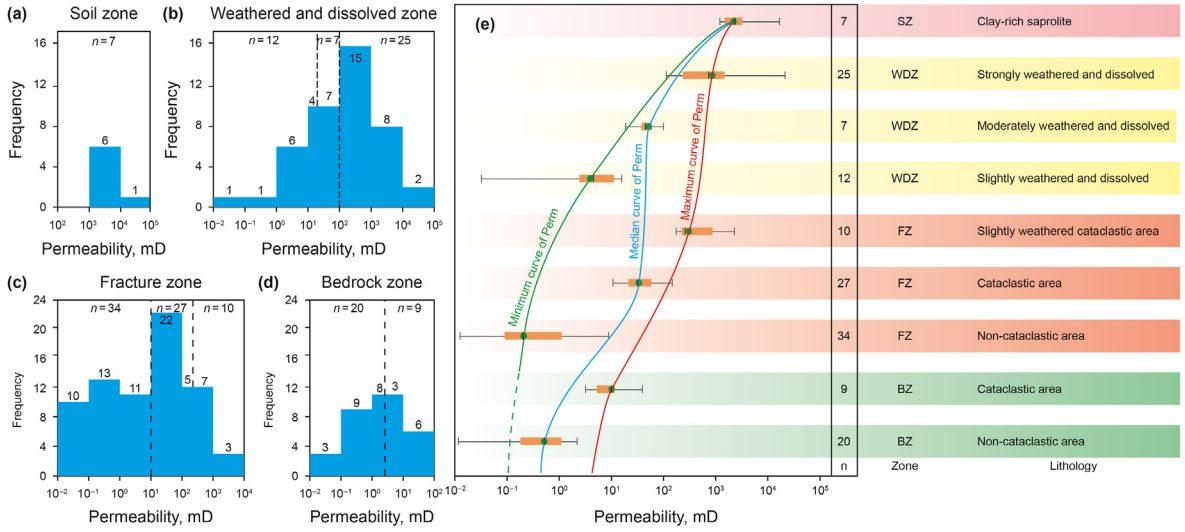

Fig. 7. Characteristics of the permeability of the Mesozoic granite in the eastern coastal area of Fujian Province (mD). (a) Permeability distribution in the soil zone. (b) Permeability distribution in the weathered and dissolved zone. (c) Permeability distribution in the fracture zone. (d) Permeability distribution in the bedrock zone. (e) Box diagram. The green, blue and red lines represent three possible trends in the field sections. The solid line is the measured data, and the dotted line is the predicted data. SZ–soil zone, WDZ–weathered and dissolved zone, FZ–fracture zone, BZ–bedrock zone.

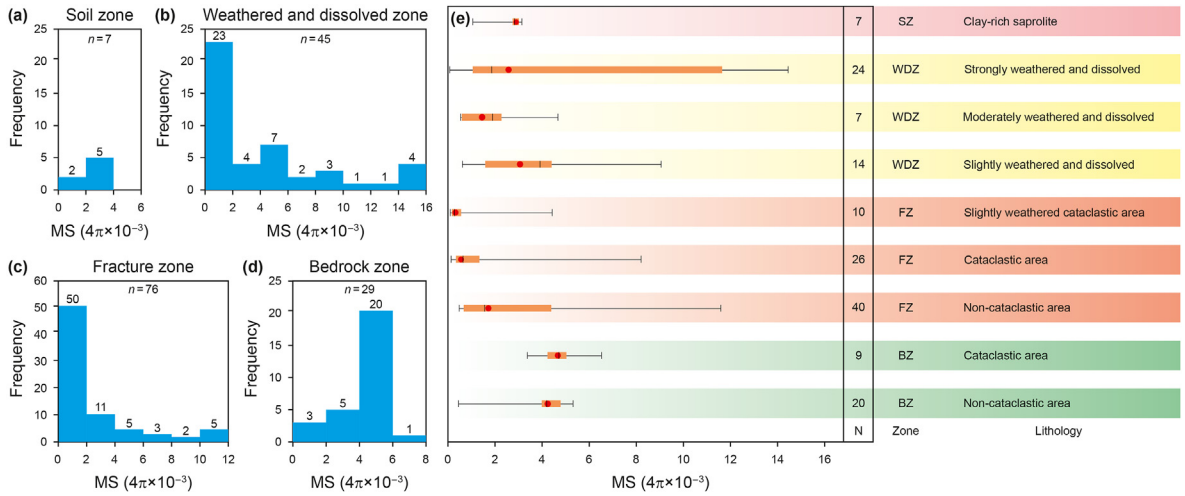

Fig. 8. Characteristics of the magnetic susceptibility of the Mesozoic granite in the eastern coastal area of Fujian Province ($4\pi \times 10^{-3}$ SI). (a) Magnetic susceptibility distribution in the soil zone. (b) Magnetic susceptibility distribution in the weathered and dissolved zone. (c) Magnetic susceptibility distribution in the fracture zone. (d) Magnetic susceptibility distribution in the bedrock zone. (e) Box diagram. SZ–soil zone, WDZ–weathered and dissolved zone, FZ–fracture zone, BZ–bedrock zone.

Table 2
Major element analysis (%) and CIA (%) of the Mesozoic granite in the eastern coastal area of Fujian Province.

Sample	SiO_2	Al_2O_3	TFe_2O_3	CaO*	MgO	K_2O	Na_2O	TiO_2	P_2O_5	MnO	LOI	Total	CIA, %
JZ-1	66.78	16.66	2.99	0.14	0.20	6.18	4.79	0.52	0.04	0.14	1.36	99.79	60.0
JZ-2	68.44	15.81	2.53	0.38	0.12	7.15	3.93	0.49	0.09	0.07	0.88	99.88	58.0
JZ-3	68.94	15.21	2.54	0.40	0.13	7.21	3.77	0.46	0.10	0.09	0.94	99.79	57.2
GW-SZ-1	72.17	14.75	2.05	0.54	0.25	4.35	4.00	0.30	0.03	0.11	1.19	99.73	62.4
GW-SZ-3	72.39	14.04	2.38	1.11	0.46	4.11	4.43	0.31	0.07	0.17	0.49	99.97	59.3
GW-CSC-1	70.29	16.05	2.63	0.41	0.27	3.79	3.60	0.36	0.02	0.14	2.20	99.76	67.3
GW-CSC-2	71.46	15.23	2.35	0.41	0.19	4.15	3.67	0.31	0.02	0.11	1.69	99.57	64.9
GW-CSC-3	72.40	14.84	2.21	0.40	0.20	3.74	4.15	0.29	0.02	0.11	1.39	99.75	64.1
GW-CSC-5	69.91	16.59	2.78	0.32	0.24	3.92	2.77	0.35	0.02	0.11	2.95	99.95	70.3
GW-CSC-6	67.13	18.05	3.26	0.30	0.26	3.90	2.11	0.39	0.02	0.10	4.36	99.89	74.1
GW-CSC-9	72.39	14.10	2.49	0.91	0.38	4.14	4.46	0.30	0.08	0.16	0.48	99.90	59.7
GW-CSC-10	72.24	14.37	2.37	0.71	0.37	4.40	4.09	0.33	0.04	0.13	0.89	99.96	61.0
XP-HWJ-1	75.95	12.70	1.67	0.24	0.08	4.60	4.08	0.12	0.01	0.13	0.36	99.95	58.7
XP-SS-1	74.34	13.57	1.82	0.16	0.16	4.75	3.39	0.20	0.03	0.08	1.14	99.64	62.0
XP-SS-2	75.20	13.26	1.34	0.19	0.14	4.83	3.64	0.17	0.02	0.05	0.85	99.69	60.5
XP-SS-5	75.12	13.32	1.70	0.17	0.14	3.88	3.33	0.19	0.02	0.09	1.89	99.84	64.4
XP-BQ-1	78.13	11.34	2.74	0.06	0.23	2.01	0.15	0.44	0.02	0.12	4.65	99.89	83.6
XP-BQ-3	74.75	13.26	1.63	0.11	0.10	5.36	2.86	0.19	0.01	0.09	1.61	99.97	61.4
XP-DJHT-1	75.07	13.25	1.45	0.34	0.14	4.56	4.10	0.16	0.02	0.06	0.63	99.79	59.5
XP-DJHT-2	74.50	13.30	1.83	0.33	0.25	4.48	4.00	0.18	0.02	0.13	0.73	99.75	60.2
XP-DJHT-3	74.99	13.21	1.51	0.30	0.17	4.78	3.83	0.16	0.02	0.11	0.82	99.92	59.7
XP-DJHT-6	82.81	8.70	1.04	0.27	0.08	4.24	1.89	0.10	0.01	0.10	0.39	99.64	57.6
XP-DJHT-9	75.28	13.92	1.41	0.06	0.17	5.18	0.37	0.14	0.01	0.05	3.04	99.63	71.3
XP-DJC-4	76.14	12.89	1.40	0.25	0.07	6.05	1.78	0.12	0.01	0.09	1.17	99.96	61.5
XP-DJC-2	69.22	16.96	2.64	0.24	0.21	4.64	1.28	0.26	0.01	0.09	4.13	99.68	73.3
XP-MF-1	67.34	15.55	3.89	3.34	1.14	3.39	3.57	0.41	0.14	0.10	0.85	99.73	60.2
XP-MF-2	67.39	15.20	4.20	2.61	1.49	3.91	2.95	0.47	0.14	0.10	1.53	99.99	61.6
XP-MF-3	67.38	14.97	4.18	2.71	1.34	3.94	3.05	0.43	0.13	0.11	1.33	99.59	60.7
XP-MF-4	67.68	15.19	3.94	2.51	1.34	3.86	2.83	0.42	0.12	0.10	1.69	99.69	62.3
XP-MF-5	68.39	15.49	3.47	2.58	1.05	3.66	3.21	0.38	0.11	0.09	1.54	99.97	62.1
XP-MF-6	67.47	15.61	4.01	2.29	1.26	3.51	3.62	0.44	0.13	0.11	1.38	99.83	62.4
XP-MF-7	67.53	15.74	4.01	2.29	1.01	3.03	3.28	0.41	0.13	0.09	2.07	99.59	64.7
XP-MF-8	67.18	15.68	3.88	2.64	1.17	3.56	3.19	0.41	0.13	0.09	1.64	99.57	62.6
XP-MF-12	68.85	14.59	3.75	2.36	1.71	1.10	4.97	0.38	0.12	0.13	1.68	99.65	63.4
XP-MF-19	64.48	16.25	4.36	3.45	1.62	3.22	3.27	0.47	0.13	0.11	2.43	99.78	62.1
XP-MF-21	69.00	15.08	3.43	1.43	0.89	3.93	4.07	0.35	0.11	0.09	1.48	99.87	61.5
FD-NLG-3	72.43	15.82	1.89	0.05	0.18	4.03	0.29	0.22	0.01	0.11	4.78	99.81	78.3
FD-NLG-4	76.04	12.97	1.32	0.12	0.11	5.76	2.17	0.18	0.01	0.08	1.21	99.98	61.7
FD-NLG-5	74.26	13.63	1.83	0.19	0.19	4.60	3.76	0.21	0.01	0.12	0.98	99.78	61.4
FD-NLG-6	73.81	13.61	1.93	0.22	0.21	4.76	3.72	0.20	0.05	0.12	1.01	99.63	61.0
FD-TMS-3	73.62	14.74	2.57	0.04	0.05	3.57	0.17	0.17	0.01	0.24	4.54	99.71	79.6
FD-TMS-4	76.23	11.59	2.08	0.25	0.10	4.59	3.81	0.14	0.01	0.19	0.53	99.52	57.3
FD-TMS-6	76.91	12.01	1.69	0.04	0.05	4.56	3.70	0.12	0.01	0.10	0.56	99.75	59.1
FD-TMS-7	77.37	11.89	1.67	0.07	0.04	4.30	3.12	0.12	0.00	0.13	1.04	99.76	61.4

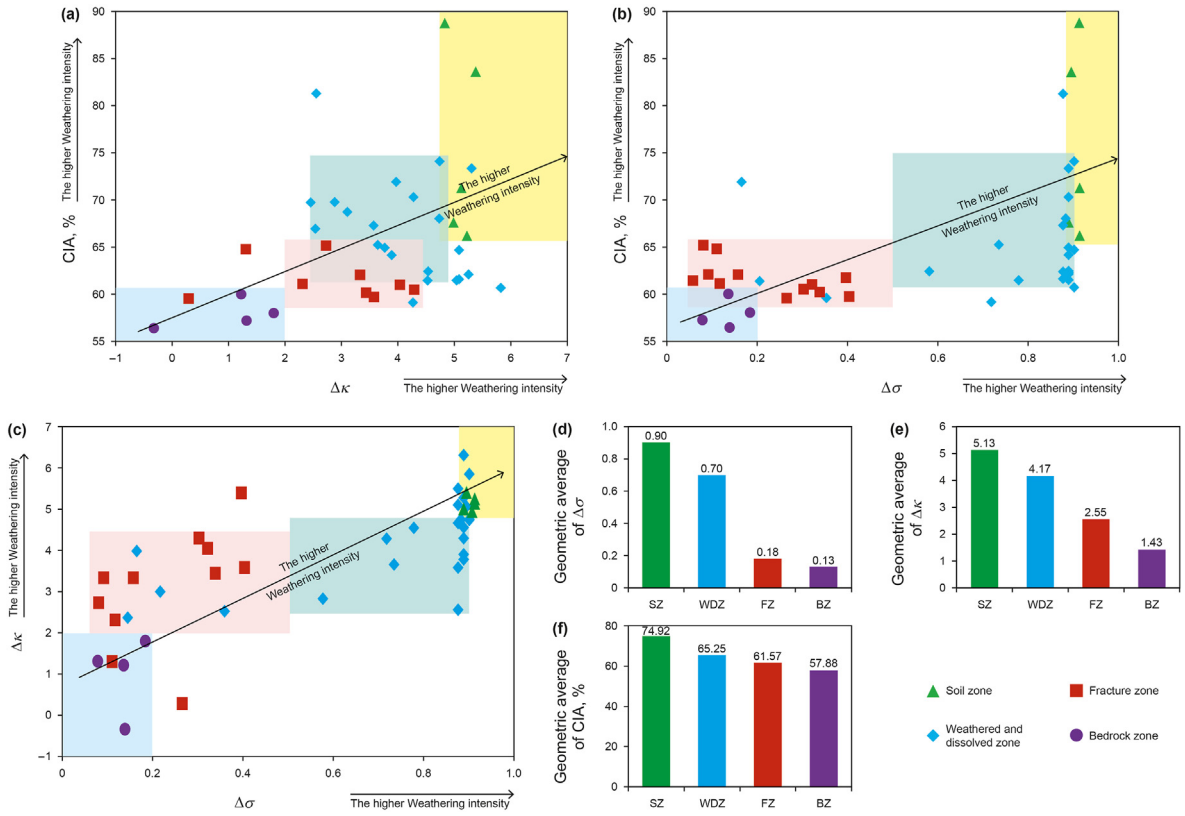

Fig. 9. Quantitative characterization of the zonation of the Mesozoic granite weathering crust in the eastern coastal area of Fujian Province. (a) Plot of $\Delta\kappa$ versus CIA. (b) Plot of $\Delta\sigma$ versus CIA. (c) Plot of $\Delta\sigma$ versus $\Delta\kappa$. (d) Geometric average of $\Delta\sigma$. (e) Geometric average of $\Delta\kappa$. (f) Geometric average of CIA. SZ–soil zone, WDZ–weathered and dissolved zone, FZ–fracture zone, BZ–bedrock zone.

Table 3
Mineral content of the Mesozoic granites in the eastern coastal area of Fujian Province. SZ-soil zone, WDZ-weathered and dissolved zone, FZ-fracture zone, BZ-bedrock zone. The blank space in the table indicates that the measured value is 0.

Sample	Quartz	Alkali feldspar	Plagioclase	Biotite	Muscovite	Calcite	Hornblende	Chlorite	Kaolinite	Illite	Montmorillonite	Zone
FD-LA-3	35	24	33					5	3			SZ
XP-DJHT-11	94					1		3	2			SZ
GWCSC-6	34	32	31	1				1	1			WZ
XP-MF-4	37	25	28	2			7				1	WZ
XP-MF-5	25	33	35	2			2				3	WZ
XP-MF-10	24	32	31	4			5	2	1	1		WZ
XP-MF-11	25	20	42	4	1			5	3			WZ
XP-MF-14	22	11	53	4				3	2		2	WZ
XP-MF-15	25	28	40	4				2	1			WZ
XP-MF-17	25	42	28	1				2	2			WZ
XP-MF-18	31	24	38	2				2	3			WZ
XP-MF-19	30	22	40	1	1			1	3	1	1	WZ
XP-DJC-2	41	24	26	1		4		1	2			FZ
FD-LA-2	37	27	32	1	2					1		FZ
FD-NLG-3	69	10	18					1	1		1	FZ
JZ-1	18	33	44	5								BZ
JZ-2	17	47	33	3								BZ
JZ-3	17	48	33	2								BZ

was 1–8%, with a geometric average of 4% (Table 3). $\Delta\kappa$ in the fracture zone ranged from 0.50 to 4.50, with a geometric average of 2.55. $\Delta\sigma$ ranged from 0.05 to 0.55, with a geometric average of 0.18. The CIA was 58.0–66.0%, with a geometric average of 61.6% (Fig. 9). The clay mineral content was 1–3%, with a geometric average of 2% (Table 3). $\Delta\kappa$ in the bedrock zone ranged from −0.50 to 2.00, with a geometric average of 1.43 (the negative value was caused by the logarithmic function, indicating that the permeability at this measuring point was close to the minimum value). $\Delta\sigma$ ranged from 0.01 to 0.20, with a geometric average of 0.13. The CIA was 55.0–61.0%, with a geometric average of 57.8% (Fig. 9). The clay mineral content was < 1% (Table 3). In conclusion, the larger the values of $\Delta\sigma$ and $\Delta\kappa$, the higher the physical and chemical weathering intensity. The higher the CIA and clay mineral content, the higher the chemical weathering intensity. Therefore, the simultaneous increases in $\Delta\sigma$, $\Delta\kappa$, and CIA indicate an increase in the physical and chemical weathering intensity.

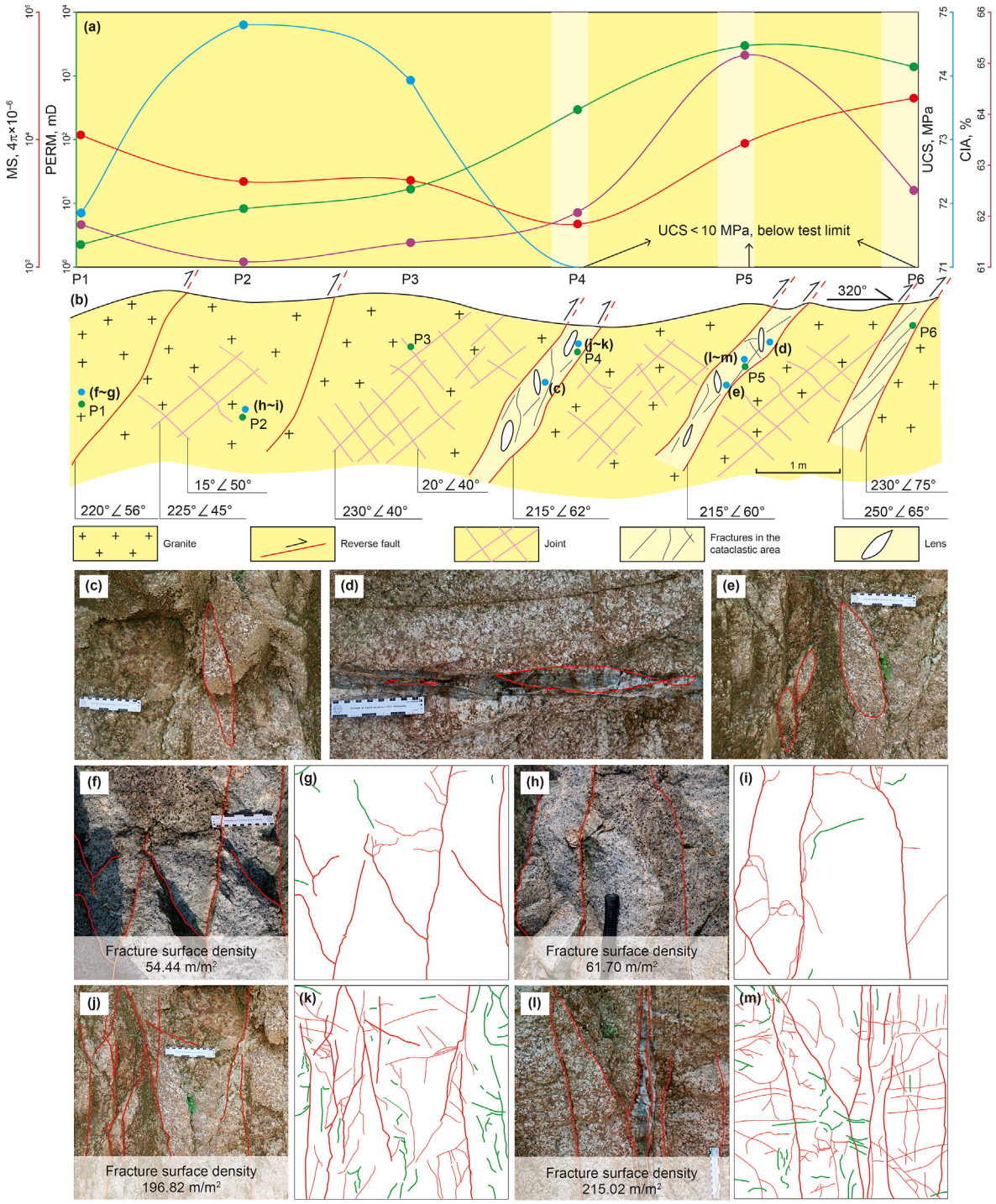

Fig. 10. Characteristics of cataclastic area of the Mingfu quarry section in the eastern coastal area of Fujian Province. (a) Physical and chemical parameters of the rocks. (b) Sketch of section. (c–e) Lens developed in the cataclastic area. (f–i) Fracture surface density in the non-cataclastic area. (j–m) Fracture surface density in the cataclastic area. The green lines in (g), (i), (k), and (m) denote the weathered fractures; the thick red lines denote the main structural fractures; and the thin red lines denote the derived structural fractures.

6. Discussion

6.1. Characteristics and function of fracture and cataclastic area in granite weathering crust

The reservoir space types of the granite weathering crust are mainly fractures and dissolution pores, among which the structural fractures provide fluid seepage channels for dissolution and the necessary conditions for weathering, thus controlling the development of the dissolution pores and weathered fractures (Liu et al., 2021). Thus, structural fractures are an important topic in granite weathering crust reservoir research. When observing and measuring the field sections, it was found that there was a certain area in the fracture and bedrock zones. In this area, structural fractures were well-developed and the rock had been cut by fractures and was seriously broken, forming rhombus-shaped blocks

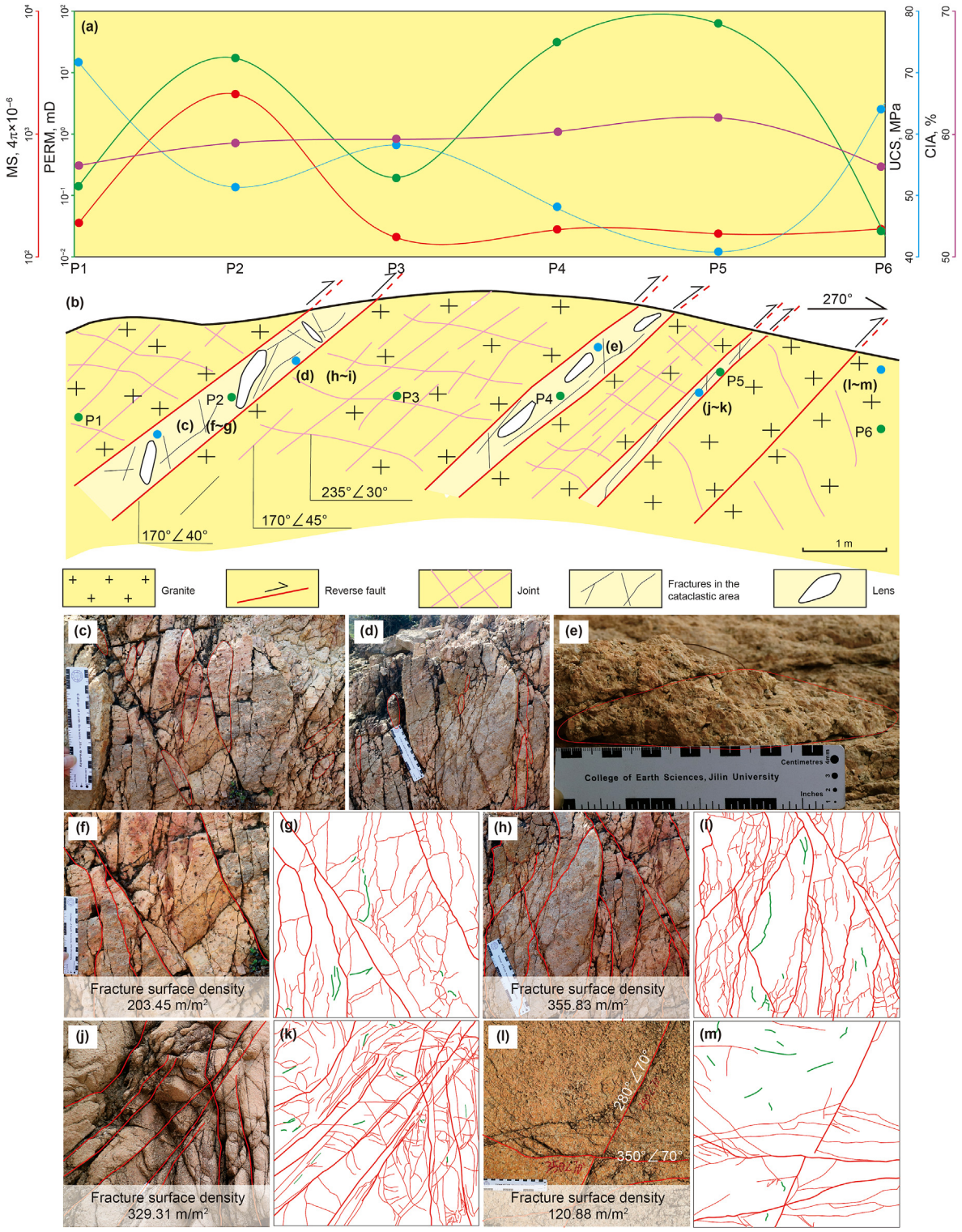

Fig. 11. Characteristics of the cataclastic area of the Niulanggang section in the eastern coastal area of Fujian Province. (a) Physical and chemical parameters of the rocks. (b) Sketch of section. (c–e) Lens developed in the cataclastic area. (f–k) Fracture surface density in the cataclastic area. (l) and (m) Fracture surface density in the non-cataclastic area. The green lines in (g), (i), (k), and (m) denote the weathered fractures; the thick red lines denote the main structural fractures; and the thin red lines denote the derived structural fractures.

and lenses. The UCS in this area was low and the permeability was high. This area was labeled the cataclastic area. Similarly, Luo et al. (2022) also proposed that a rock bridge was developed in the widely distributed granite in the crust, which was characterized by discontinuity of the structural plane, a high strength, stress concentration, and brittle failure. Due to the heterogeneity of the lithology and fractures, Luo et al.'s (2022) rock bridge area is similar to the cataclastic area proposed in this paper. Taking the outcrops in

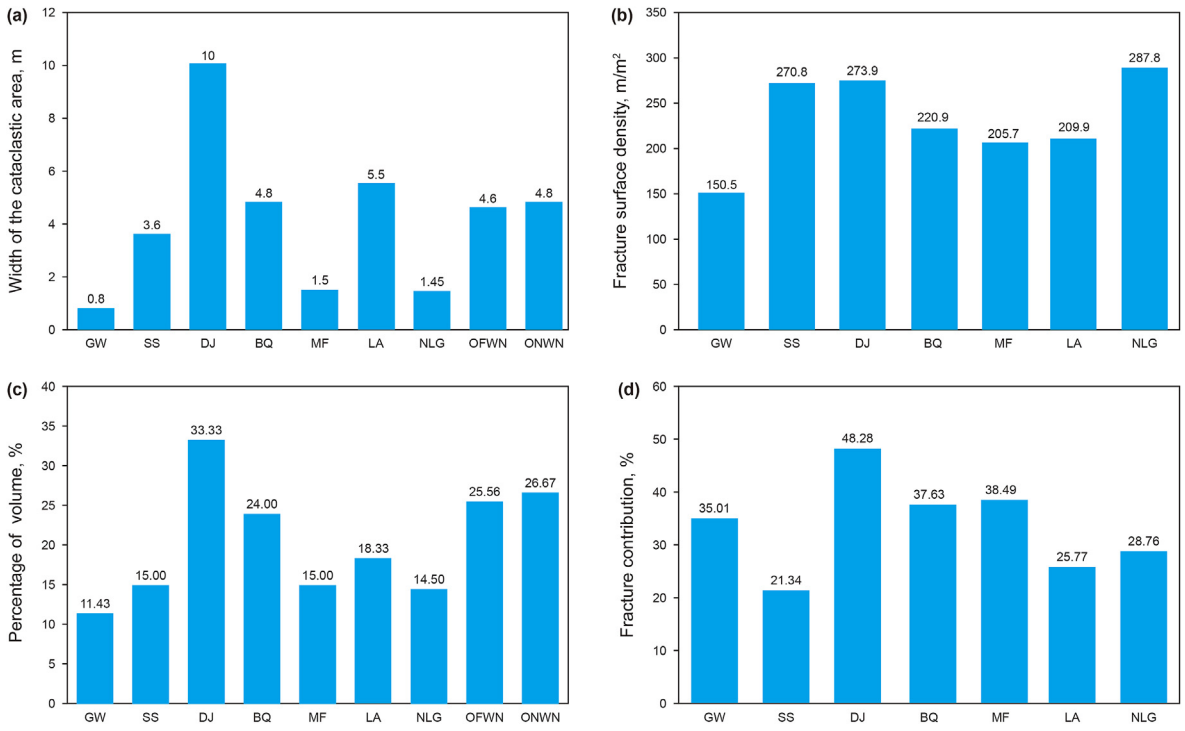

Fig. 12. Characteristics of the cataclastic area in the Mesozoic granite weathering crust in the eastern coastal area of Fujian Province. (a) Width of the cataclastic area. (b) Fracture surface density of the cataclastic area. (c) Proportion of the cataclastic area in the rock mass volume. (d) Percentage of fractures contributed by the cataclastic area. GW: Guwei sluice, Lianjiang County. SS: Sansha Town, Xiapu County. DJ: Dajing beach, Xiapu County. BQ: Beiqi Village, Xiapu County. MF: Mingfu quarry, Xiapu County. LA: Long'an, Fuding City. NLG: Niulanggang, Fuding City. OFWN: Offshore of western Norway. ONWN: Onshore in western Norway. OFWN and ONWN are from Alberto et al. (2021).

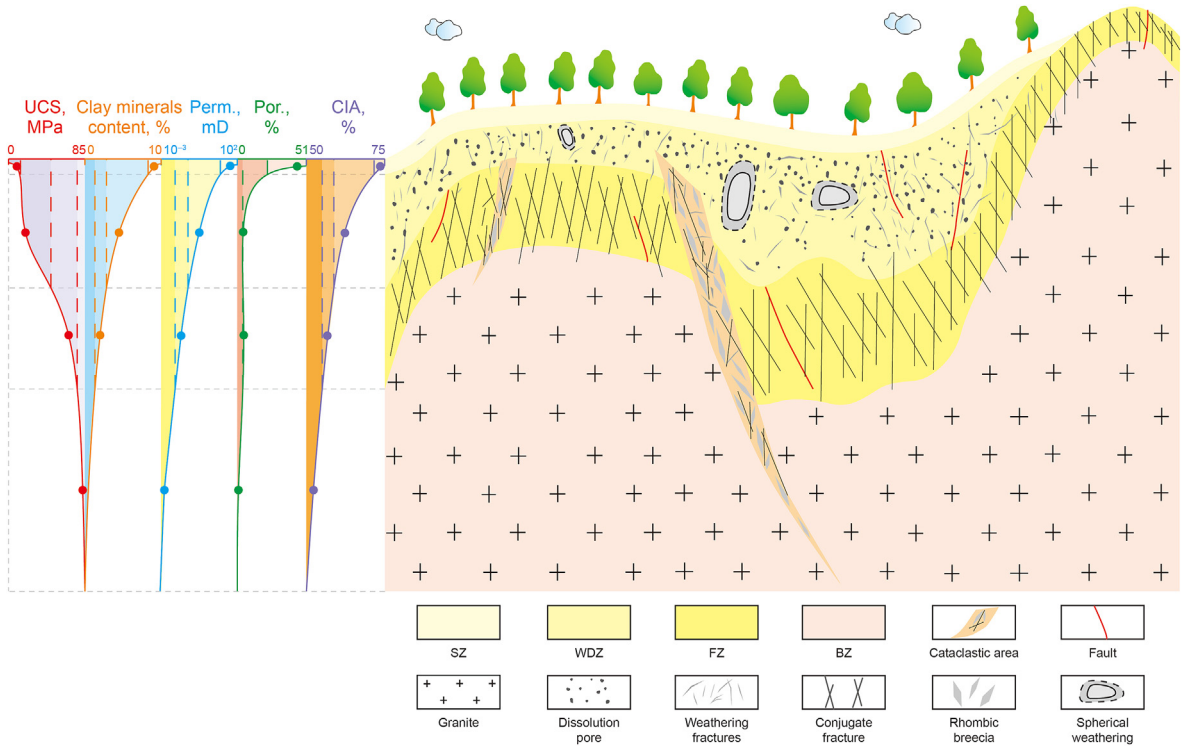

Fig. 13. Physical properties of the Mesozoic granite reservoirs in the eastern coastal area of Fujian Province. The dotted lines in different colors represent the cutoff values of each key sensitive parameter in each zonation. The different colored circles represent the average values of the parameters in each zone. SZ–soil zone, WDZ–weathered and dissolved zone, FZ–fracture zone, BZ–bedrock zone.

Mingfu quarry in Lianjiang County and Niulanggang in Fuding City as examples, the reasons for the characteristics of the rocks and

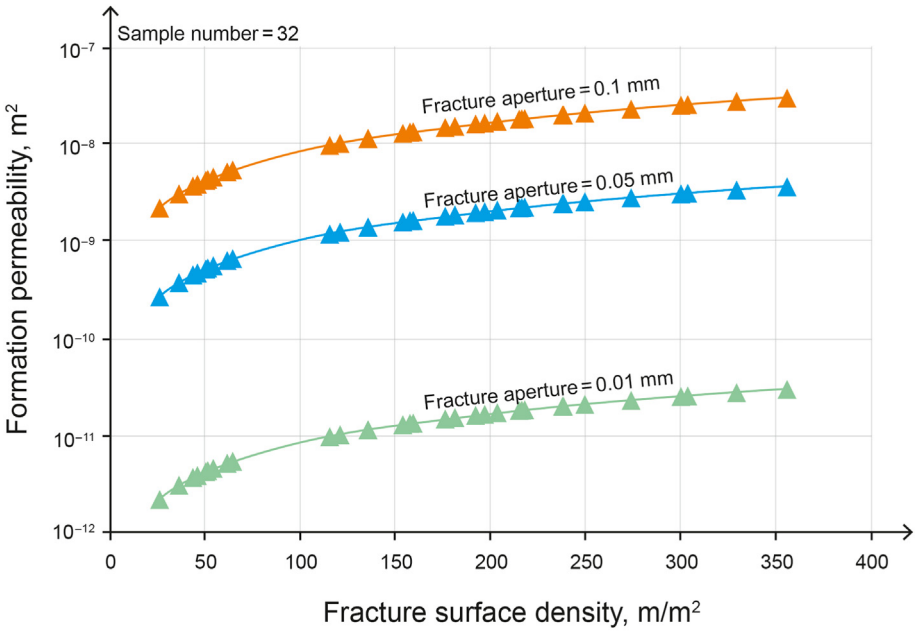

Fig. 14. Permeability simulation conducted using the fracture intensity per area of granite weathering crust in the eastern coastal area of Fujian Province.

fractures in the cataclastic area were deduced, and the role of the cataclastic area in the reservoir's development was analyzed through statistical analysis of the data for all of the sampling locations.

6.1.1. Characteristics of cataclastic area of outcrop in Mingfu quarry

The outcrop in Mingfu quarry exhibited the characteristics of the cataclastic area of the granite weathering crust. Six measurement points were selected horizontally along this outcrop to measure the magnetic susceptibility, permeability, and uniaxial compressive strength of the rock (Fig. 10a). The six measurement points in this section were labeled P1, P2, P3, P4, P5, and P6. It was found that the UCS values at measurement points P4, P5, and P6 were lower than the test range of the instrument (< 10 MPa), and the permeabilities at these three points were higher than those at P1, P2, and P3. Lenses were developed at points P4, P5, and P6 (Fig. 10b–10e). Therefore, this area was defined as the cataclastic area. The six measurement points were photographed and sampled, and then major element analysis was carried out on the samples and their CIA values were calculated. Then, the photos were examined, and the outcrop surfaces with the same field of view were used to calculate the fracture surface density statistics (the ratio of the total length of the fractures in the field of view to the area of the field of view).

The measurements and statistical results revealed that the CIA values were higher at measurement points P4, P5, and P6 than at P1, P2, and P3 (Fig. 10a). The fracture surface density at point P1 was about 54.44 m/m^2 (Fig. 10f and 10g), the fracture surface density at point P2 was about 61.70 m/m^2 (Fig. 10h and 10i), while the fracture surface density at point P4 was about 196.82 m/m^2 (Fig. 10j and 10k), and the fracture surface density at point P5 was about 215.02 m/m^2 (Fig. 10l and 10m). Based on the field survey data, it was determined that P4, P5, and P6 were located in the cataclastic area of the fracture zone.

6.1.2. Characteristics of cataclastic area of outcrop in Niulanggang

The outcrop in Niulanggang also exhibited the characteristics of the cataclastic area of the granite weathering crust. Six measurement points were selected horizontally along this outcrop to measure the magnetic susceptibility, permeability, and uniaxial compressive strength of the rock (Fig. 11a). The six measurement points in this section were labeled P1, P2, P3, P4, P5, and P6. According to the outcrop observations, the rocks at P2, P4, and P5 had been cut by fractures and were seriously broken, with many fractures and lenses developed. Therefore, this area was defined as the cataclastic area (Fig. 11b–e). Furthermore, based on the measurements, the changes in the strength of the rock from point P1 to point P6 were as follows: decrease (P1–P2) → increase (P2–P3) → decrease (P3–P5) → increase (P5–P6). The changes in the permeability exhibited the opposite pattern.

Then, the photos were examined, and the outcrop surfaces with the same field of view were used to calculate the fracture surface density statistics. The measurements and statistical results revealed that the CIA values were slightly higher at P2, P4, and P5 points than at the other three measurement points (Fig. 11a). The fracture surface density at point P2 was about 203.45–355.83 m/m^2 (Fig. 11f–i), the fracture surface density at point P5 was about 329.31 m/m^2 (Fig. 11j and 11k), and the fracture surface density at point P6 was about 120.88 m/m^2 (Fig. 11l and 11m). Based on the field survey data, it was found that P2, P4, and P5 were located in the cataclastic area of the fracture zone.

6.1.3. Role of cataclastic area in reservoir development

Among all of the outcrops observed in the field, seven contained cataclastic areas. To study the role of the cataclastic areas in the reservoir's development, in this study, the width of the cataclastic area (m), the fracture face density of the cataclastic area (m/m^2), the proportion of the cataclastic area to the rock mass volume (%), and the fracture contribution (%) of several outcrop cataclastic areas were counted and calculated.

The results revealed that the width of the cataclastic area in the fracture zone was several meters (Fig. 12a). The geometric average value of the fracture surface density was 150.50–287.80 m/m^2, and it was usually > 200.00 m/m^2 (Fig. 12b). When combined, the cataclastic areas developed in different locations in the same outcrop had a scale of tens of meters, accounting for about 20% of

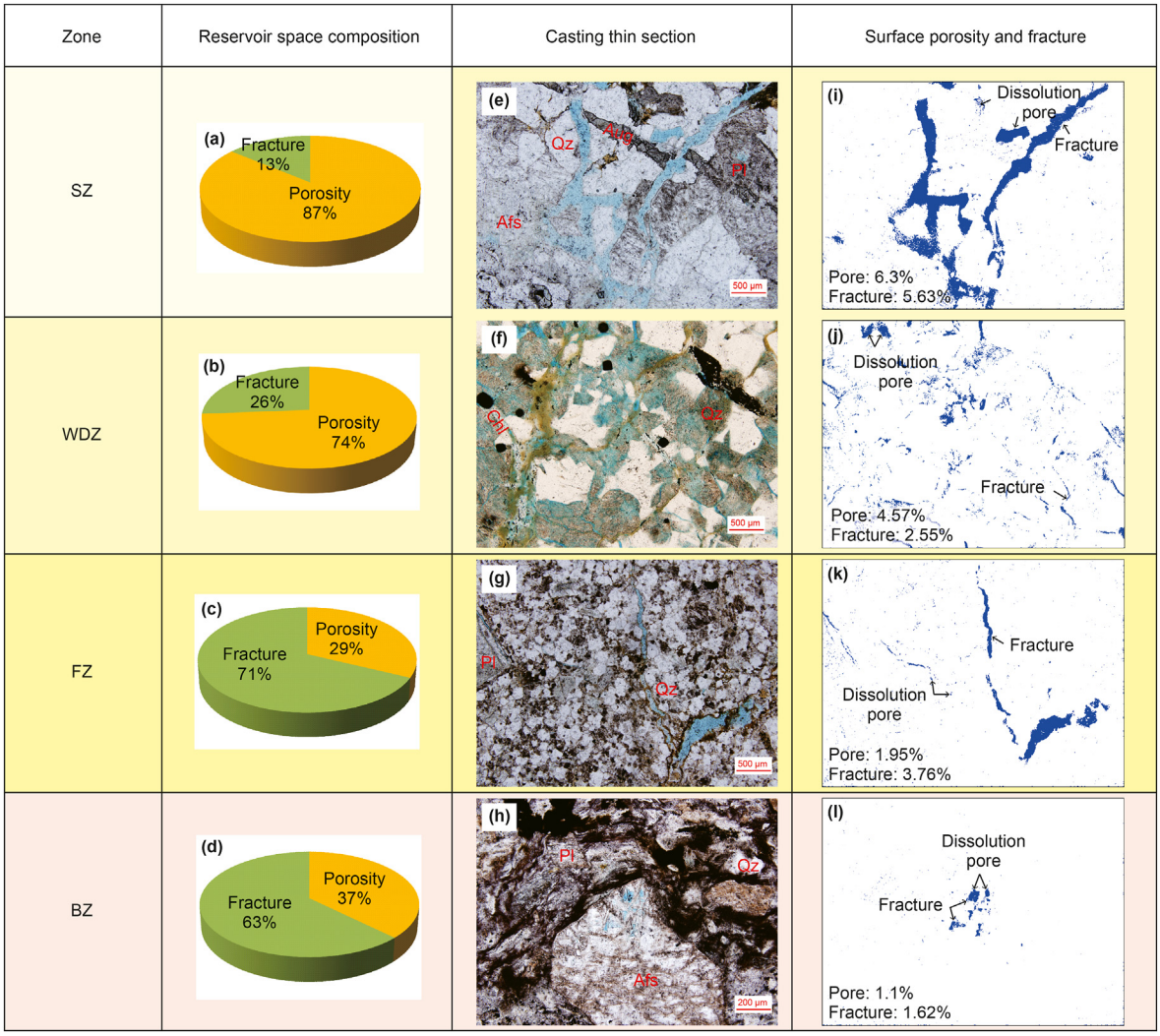

Fig. 15. Reservoir space composition of the Mesozoic granite in the eastern coastal area of Fujian Province. (a) Reservoir space composition of the soil zone, 10 casting thin sections. (b) Weathered and dissolved zone, 28 casting thin sections. (c) Fracture zone, 16 casting thin sections. (d) Bedrock zone, 3 casting thin sections. (e) and (i) Analysis results of the casting thin section and surface porosity and fracture for sample XP-MF-4, weathered and dissolved zone; (f) and (j) Sample XP-SS-3, weathered and dissolved zone; (g) and (k) Sample GWSZ-1, fracture zone; (h) and (l) Sample JZ-3, bedrock zone. SZ–soil zone, WDZ–weathered and dissolved zone, FZ–fracture zone, BZ–bedrock zone.

Table 4
Surface porosity and fracture by image analysing results for the Mesozoic granite in the eastern coastal area of Fujian Province. SZ–soil zone, WDZ–weathered and dissolved zone, FZ–fracture zone, BZ–bedrock zone.

Zone	Geometric average of surface porosity, %	Geometric average of surface fracture, %	Total porosity, %
SZ	9.83	1.42	11.25
WDZ	4.56	0.93	5.49
FZ	0.71	1.76	2.47
BZ	0.75	1.26	2.01

the volume of the rock mass (Fig. 12c). The contribution of the cataclastic area to the fractures in the rock mass could reach about 33% and was even up to about 50% in some areas (Fig. 12d). Moreover, two outcrops in western Norway have also been reported to contain cataclastic areas, with widths of several meters and a combined scale of tens of meters, which is similar to the characteristics of the cataclastic areas in our study area (Alberto et al., 2021). Therefore, it is concluded that the cataclastic area can serve as the sweet spot in the buried-hill reservoir.

The conclusion of the cataclastic area can provide geological basis for the study of the granite buried hill in the East China Sea Basin.

6.2. Reservoir physical property characteristics of granite weathering crust

As was previously mentioned, the granite weathering crust was vertically divided into four zones in this study. Samples of each zone were collected and columnar samples were drilled for the porosity and permeability analyses and to analyze the physical properties of each zone. The relevant tests were conducted at Jilin University. The rock in the soil zone was relatively soft, so it was impossible to obtain columnar samples. Therefore, the initial porosity of the rock in the soil zone calculated during the compaction test was taken as the porosity of the rock in this zone

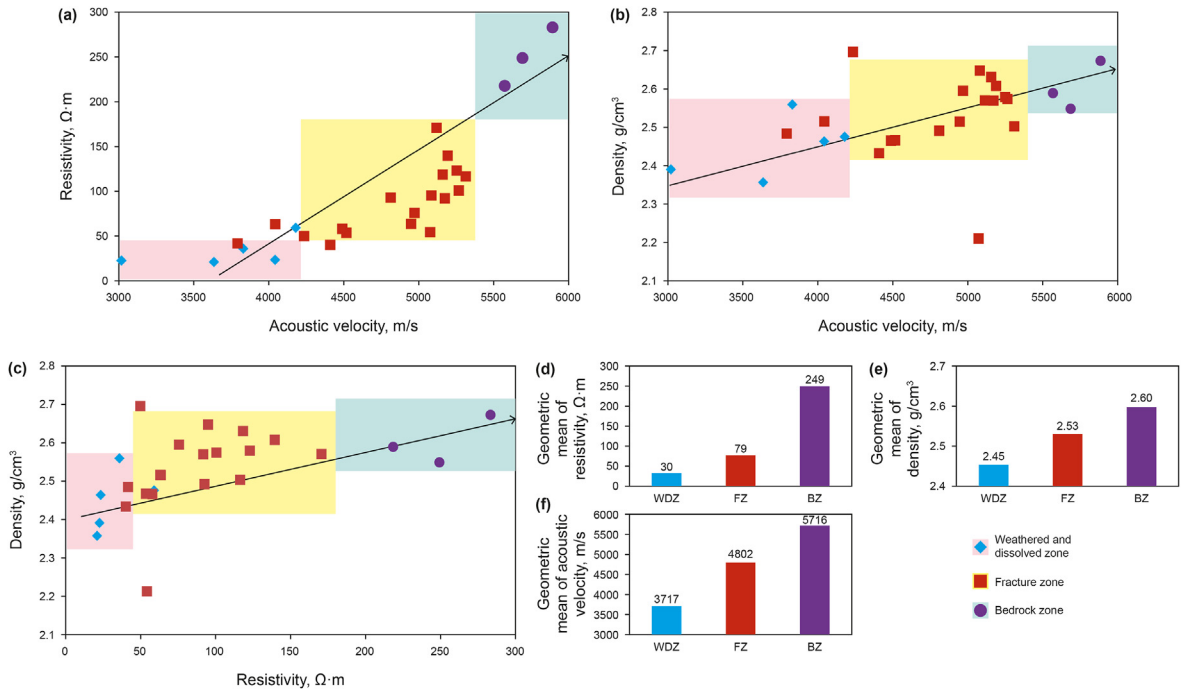

Fig. 16. Density, resistivity, and acoustic velocity of the Mesozoic granites in the eastern coastal area of Fujian Province. (a) Plot of resistivity versus acoustic velocity. (b) Plot of density versus acoustic velocity. (c) Plot of density versus resistivity. (d) Geometric average of resistivity. (e) Geometric average of density. (f) Geometric average of acoustic velocity. WDZ–weathered and dissolved zone, FZ–fracture zone, BZ–bedrock zone.

(Fisher et al., 1999; Nakata et al., 2001; Karner et al., 2003; Bernaud et al., 2006; Marcussen et al., 2010). The test results show that the porosity of the soil zone was the highest, ranging from 34.32% to 50.47%, with a geometric average value of 42.56%. The porosity of the weathered and dissolved zone was 2.44–7.52%, with a geometric average value of 4.17%; and the permeability was 0.009–10.913 mD, with a geometric average value of 0.244 mD. The porosity of the fracture zone was 2.09–9.99%, with a geometric average value of 4.62%; and the permeability was 0.011–0.325 mD, with a geometric average value of 0.053 mD. The porosity of the bedrock zone was 0.76–1.01%, with a geometric average value of 0.91%; and the permeability was 0.004–0.006 mD, with a geometric average value of 0.005 mD (Fig. 13). Due to the heterogeneity of the fracture zone, its permeability was related to fracture width and fracture surface density. In this study, based on the measured fracture surface density of the outcrop, the empirical formula:

$$k = D \times h^3 / 12, \quad (5)$$

where k is the formation's permeability (m^2); D is the fracture intensity (m/m^2); and h is the fracture aperture (m). The formula was used to analyze the permeability of the granite based on the assumed fracture aperture (Zimmerman and Bodvarsson, 1996). Fracture apertures of 0.01 mm, 0.05 mm, and 0.1 mm were assumed. If the fracture aperture was 0.01 mm, the formation's permeability was 2.18×10^{-12}–2.97×10^{-11} m^2. If the fracture aperture was 0.05 mm, the formation's permeability was 2.72×10^{-10}–3.71×10^{-9} m^2. If the fracture aperture was 0.1 mm, the formation's permeability was 2.18×10^{-9}–2.97×10^{-8} m^2 (Fig. 14). Based on the characteristics of the UCS, the clay mineral content and CIA of each zone were obtained. Although the pores of the soil zone were developed, the mineral alteration phenomenon was serious, the clay content was high, and plant roots were developed, so the physical properties of the reservoir were poor in this zone. The rock in the bedrock zone was dense, and pores were not developed, so the physical properties of the reservoir were poor in this zone. Dissolution pores were developed in the weathered and dissolved zone. The reservoir space types were mainly pore type and pore-fracture type. Fractures were developed in the fracture zone. The reservoir space types were mainly fracture type and fracture-pore type. The physical properties of these two zones were better than those of the soil and bedrock zones.

When the samples were sent back to the laboratory for analysis of the reservoir physical property, casting thin sections were also made, and thin section porosity and fracture quantification were conducted to determine the pore composition characteristics of each zone. The analysis results revealed that the geometric average value of the surface porosity of the soil zone was 9.83%, the geometric average value of the surface fractures was 1.42%, the total porosity was 11.25%, and the reservoir space was composed of 87% pores and 13% fractures (Fig. 15a, Table 4). The geometric average value of the surface porosity of the weathered and dissolved zone was 4.56%, the geometric average value of the surface fractures was 0.93%, the total porosity was 5.49%, and the reservoir space was composed of 74% pores and 26% fractures (Fig. 15b, Table 4). The geometric average value of the surface porosity of the fracture zone was 0.71%, the geometric average value of the surface fractures was 1.76%, the total porosity was 2.47%, and the reservoir space was composed of 29% pores and 71% fractures (Fig. 15c, Table 4). The geometric average value of the surface porosity of the bedrock zone was 0.75%, the geometric average value of the surface fractures was 1.26%, the total porosity was 2.01%, and the reservoir space was composed of 37% pores and 63% fractures (Fig. 15d, Table 4).

6.3. Petrophysical property response of granite weathering crust zonation

The zonation of the weathering crust is particularly important for research on granite buried hills in basins around the world, and it provides important information for oil and gas exploration and

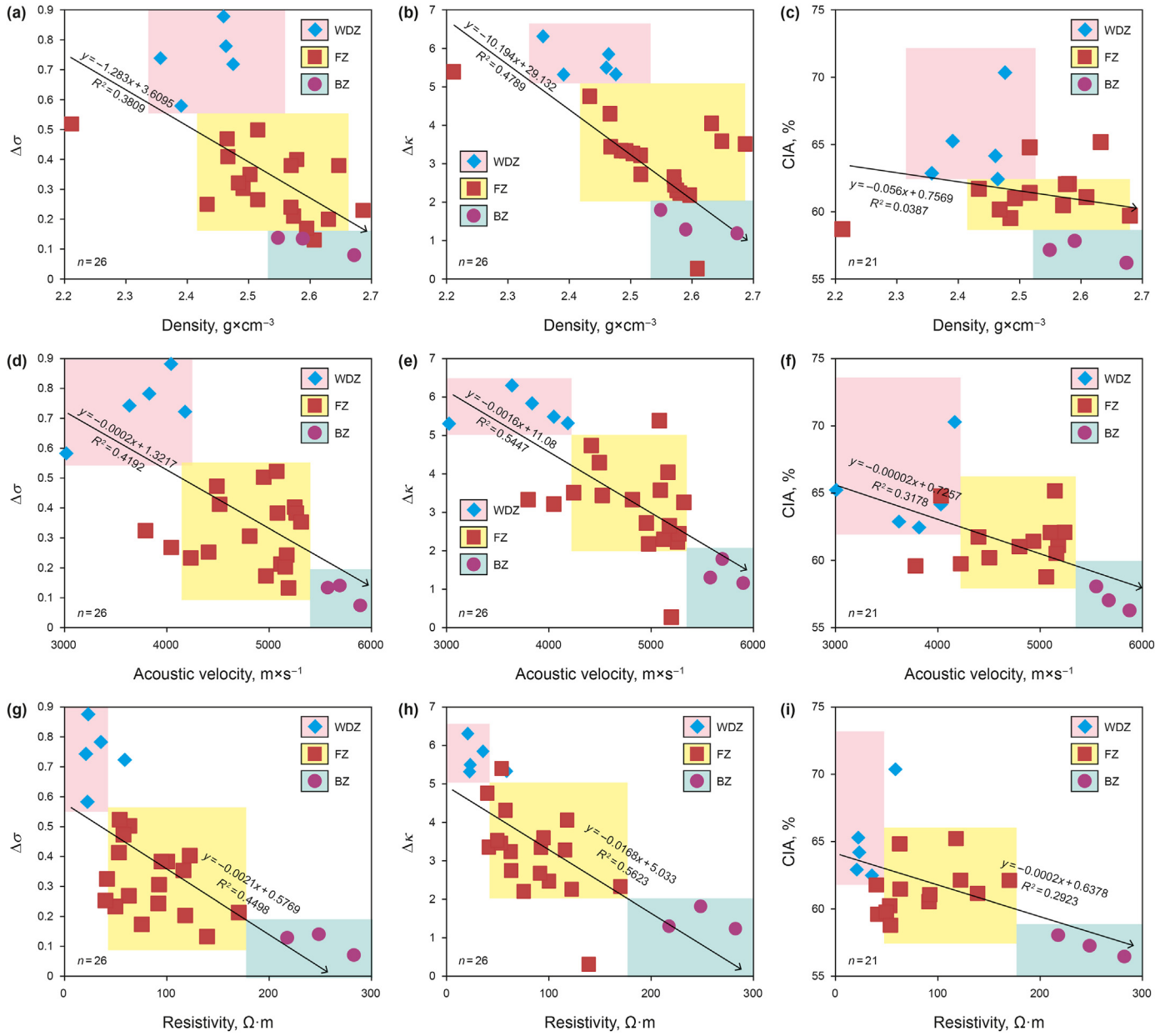

Fig. 17. Intersection plots of physical and mechanical parameters of Mesozoic granite in eastern coastal area of Fujian Province. (a) Plot of $\Delta\sigma$ versus density. (b) Plot of $\Delta\kappa$ versus density. (c) Plot of CIA versus density. (d) Plot of $\Delta\sigma$ versus acoustic velocity. (e) Plot of $\Delta\kappa$ versus acoustic velocity. (f) Plot of CIA versus acoustic velocity. (g) Plot of $\Delta\sigma$ versus resistivity. (h) Plot of $\Delta\kappa$ versus resistivity. (i) Plot of CIA versus resistivity.

development. Studies have shown that the logging curve is an indispensable basis for dividing buried hills into zones (Hu et al., 2017; Dou et al., 2018; Ye et al., 2020a). Therefore, the density, resistivity, and acoustic velocity were selected to test and analyze the granite columnar samples. The results revealed that similar to the UCS, permeability, and CIA, the single parameter classification effect was not good, but the use of a combination of parameters can achieve a better classification effect. As is shown in Fig. 16, in the weathered and dissolved zone, the acoustic velocity of the rock was 3000–4200 m/s, with a geometric average value of 3717 m/s; the resistivity was 0–45 Ω m, with a geometric average value of 30 Ω m; and the density was 2.32–2.57 g/cm^3, with a geometric average of 2.45 g/cm^3. In the fracture zone, the acoustic velocity of the rock was 4200–5400 m/s, with a geometric average value of 4802 m/s; the resistivity was 45–180 Ω m, with a geometric average value of 79 Ω m; and the density was 2.42–2.68 g/cm^3, with a geometric average of 2.53 g/cm^3. In the bedrock zone, the acoustic velocity of the rock was 5400–6000 m/s, with a geometric average value of 5716 m/s; the resistivity was 180–300 Ω m, with a geometric average value of 249 Ω m; and the density was 2.53–2.72 g/cm^3, with a geometric average of 2.60 g/cm^3. That is, the density, resistivity, and acoustic velocity all decreased with increasing weathering intensity. To support this view, the intersection plots of the density, resistivity, and acoustic velocity with $\Delta\kappa$, $\Delta\sigma$, and CIA, i.e., the indicators of vertical zonation mentioned above, were created. The results show that (Fig. 17) the density, resistivity, and acoustic velocity are inversely proportional to $\Delta\kappa$, $\Delta\sigma$, and CIA, respectively, indicating that these three indexes are helpful in the classification of the vertical zonation. The distribution ranges of the relevant parameters can provide a basis for vertical

zonation of and oil exploration in the granite weathering crust buried hill reservoir.

7. Conclusions

The granite weathering crust reservoir in the eastern coastal area of Fujian Province has obvious vertical zonation, with four zones from top to bottom: a soil zone, a weathered and dissolved zone, a fracture zone, and a bedrock zone. The rocks in the soil zone are loose and porous and can even be covered by vegetation. The rocks in the weathered and dissolved zone have been obviously affected by physical and chemical weathering dissolution, and weathering fractures and dissolution pores have been developed. The rocks in the fracture zone have been affected by tectonic movement and physical weathering, and structural fractures and a few weathering fractures have been developed. Affected by tectonic movement, the bedrock zone contains a cataclastic area, and fractures have been developed in this area. The rocks in the non-cataclastic area are whole and solid. The uniaxial compressive strength of the granite weathering crust gradually increases from top to bottom and the permeability gradually decreases. The fracture zone and bedrock zone contain cataclastic areas, which contribute greatly to the development of fractures in the rock mass and serve as the sweet spot of the reservoir.

A combination of multiple parameters (i.e., the rate of change of the uniaxial compressive strength, the rate of change of the permeability, and the CIA) was applied to determine the zonation of the granite weathering crust, and good results were achieved. The rate of change of the uniaxial compressive strength ($\Delta\sigma$), the rate of change of the permeability ($\Delta\kappa$), and CIA increased gradually from bottom to top, indicating a gradual increase in the physical and chemical weathering intensity.

Based on the petrophysical parameters of the rocks, including the density, resistivity, and acoustic velocity, a good division effect of the rock parameters in each zone was achieved. The results of this study provide a basis for the zonation of the granite buried-hill weathering crust and oil and gas exploration in the East China Sea Basin.

Declaration of competing interest

The authors declare that they have no known competing financial interests or personal relationships that could have appeared to influence the work reported in this paper.

Acknowledgements

This work was supported by the Key Research and Development Program of Jilin Province (grant No.20230203107SF), the National Natural Science Foundation of China (Grant No. 41790453), the National Key Research and Development Program of China (Grant No. 2019YFC0605402), and the National Major Science and Technology Project of the Ministry of Science and Technology of China (Grant No. 2016ZX05026-004-001).

References

Abdunaser, K.M., 2015. Review of the petroleum geology of the western part of the Sirt Basin, Libya. J. Afr. Earth Sci. 111, 76–91. https://doi.org/10.1016/j.jafrearsci.2015.07.005.

Alberto, C., Giulio, V., Giulia, T., et al., 2021. In–situ quantification of mechanical and permeability properties on outcrop analogues of offshore fractured and weathered crystalline basement: examples from the Rolvsnes granodiorite, Bømlo, Norway. Mar. Petrol. Geol. 124, 104859. https://doi.org/10.1016/j.marpetgeo.2020.104859.

Alsharhan, A.S., 2003. Petroleum geology and potential hydrocarbon plays in the Gulf of Suez rift basin, Egypt. AAPG Bull. 87 (1), 143–180. https://doi.org/10.1306/062002870143.

Aydin, A., Basu, A., 2005. The Schmidt hammer in rock material characterization. Eng. Geol. 81 (1), 1–14. https://doi.org/10.1016/j.enggeo.2005.06.006.

Bernaud, D., Dormieux, L., Maghous, S., 2006. A constitutive and numerical model for mechanical compaction in sedimentary basins. Comput. Geotech. 33 (6–7), 316–329. https://doi.org/10.1016/j.compgeo.2006.05.004.

Cuong, T.X., Warren, J.K., 2009. Bach Ho field, a fractured granitic basement reservoir, Cuu Long Basin, offshore SE Vietnam: a "buried-hill" play. J. Petrol. Geol. 32 (2), 129–156. https://doi.org/10.1111/j.1747-5457.2009.00440x.

Dou, L.R., Xiao, K.Y., Hu, Y., et al., 2011. Petroleum geology and a model of hydrocarbon accumulations in the Bongor Basin, the Republic of Chad. Acta Pet. Sin. 32 (3), 379–386. https://doi.org/10.7623/syxb201103002 (in Chinese).

Dou, L.R., Wei, X.D., Wang, J.C., et al., 2015. Characteristics of granitic basement rock buried hill reservoir in Bongor Basin, Chad, 925 Acta Pet. Sin. 36 (8), 897–904. https://doi.org/10.7623/syxb201103002 (in Chinese).

Dou, L.R., Wang, J.C., Wang, R.C., et al., 2018. Precambrian basement reservoirs: case study from the northern Bongor Basin, the Republic of Chad. AAPG Bull. 102 (9), 1803–1824. https://doi.org/10.1306/02061817090.

Ellis, A.C., Kerr, H.M., Cornwell, C.P., et al., 1996. A tectono-stratigraphic framework for Yemen and its implications for hydrocarbon potential. Petrol. Geosci. 2 (1), 29–42. https://doi.org/10.1144/petgeo.2.1.29.

El-Naby, A.A., El-Aal, M.A., Kuss, J., et al., 2009. Structural and basin evolution in Miocene time, southwestern Gulf of Suez, Egypt. Egypt. Neues Jahrbuch Geol. Palaontol. Abhand. 251 (3), 331–353. https://doi.org/10.1127/0077-7749/2009/0251-0331.

Eshanibli, A., Khalil, A., Younis, A., et al., 2020. Structural framework of the zelten platform, south sirte basin, Libya using potential fields modelling. Acta Geodyn. Geomater. 17 (2), 229–236. https://doi.org/10.13168/AGG.2020.0017.

Fisher, Q.J., Casey, M., Clennell, M.B., et al., 1999. Mechanical compaction of deeply buried sandstones of the North Sea. Mar. Petrol. Geol. 16 (7), 605–618. https://doi.org/10.1016/S0264-8172(99)00044-6.

Gruenwald, R., 2001. The hydrocarbon prospectivity of lower oligocene deposits in the maragh trough, SE Sirt basin, Libya. J. Petrol. Geol. 24 (2), 213–231. https://doi.org/10.1111/j.1747-5457.2001.tb00668x.

Harris, R., Cooper, M., Shook, I., 2002. Structural analysis in eastern Yemen using remote sesing data. World Oil 223 (11), 52–56. https://doi.org/10.1306/61eeea98-173e-11d7-8645000102c1865d.

Hou, M.C., Cao, H.Y., Li, H.Y., et al., 2019. Characteristics and controlling factors of deep buried-hill reservoirs in the BZ19-6 structural belt, Bohai Sea area. Nat. Gas. Ind. 39 (1), 33–44. https://doi.org/10.3787/j.issn.1000-0976.2019.01.004 (in Chinese).

Hu, Y., 2014. Crustal Deformation Characteristics and Mantle Dynamics Analysis Research of Southeast Coastal Areasin Fujian Province. Dissertation. Chang'an University, Xi'an. https://doi.org/10.7666/d.D558109 (in Chinese).

Hu, Z.W., Xv, C.G., Yang, B., et al., 2017. Reservoir forming mechanism of Penglai 9-1 granite buried-hills and its oil geology significance in Bohai Sea. Acta Pet. Sin. 38 (3), 274–285. https://doi.org/10.7623/syxb201703004 (in Chinese).

Karner, S.L., Chester, F.M., Kronenberg, A.K., et al., 2003. Subcritical compaction and yielding of granular quartz sand. Tectonophysics 377 (3–4), 357–381. https://doi.org/10.1016/j.tecto.2003.10.006.

Koning, T., 2003. Oil and gas production from basement reservoirs: examples from Indonesia , USA and Venezuela. Geol. Soc. Spec. Publ. 16, 250–251. https://doi.org/10.1144/GSL.SP.2003.214.01.05.

Koning, T., 2020. Giant and major-size oil and gas fields worldwide in basement reservoirs: state-of-the-art and future prospects. Georesursy 40–48.. https://doi.org/10.18599/grs.2020.SI.40-48.

Li, H.Y., Cai, H.T., Jin, X., et al., 2021. Analysis of the crustal thickness and Poisson's ratio in Fujian, Southeast China, from teleseismic P-wave receiver functions. Chin. J. Geophys. 64 (3), 805–822. https://doi.org/10.6038/cjg2021N0431 (in Chinese).

Li, J.P., Zhou, X.H., Wang, G.Z., 2014. Lithologic constitution and its control on reservoir development on Penglai 9-1 buried hill, Bohai Bay Basin. J. Earth Sci. 39 (10), 1521–1530. https://doi.org/10.3799/dqkx.2014.134 (in Chinese).

Li, S.N., Ni, P., Bao, T., et al., 2018. Geology, fluid inclusion, and stable isotope systematics of the Dongyang epithermal gold deposit, Fujian Province, southeast China; implications for ore genesis and mineral exploration. J. Geochem. Explor. 195, 16–30. https://doi.org/10.1016/j.gexplo.2018.02.009.

Li, Y.T., Hou, Q.Y., Xiao, Y., 2022. Geochemical compositions and detrital minerals of stream sediments around the Zijinshan copper-gold orefield and their implications. Minerals 12 (1), 39–50. https://doi.org/10.3390/min12010032.

Liu, Y.H., Yu, X.Z., Li, J., 2007. Magnetic characteristics of different types of granite in Southeast coastal area of China. Geophys. Geochem. Explor. 31 (6), 526–528. https://doi.org/10.3969/j.issn.1000-8918.2007.06.011 (in Chinese).

Liu, Z., Zhu, M.L., Liu, H.M., et al., 2021. Formation mechanism and distribution characteristics of granite weathering crust reservoir: a case study of the western segment of the northern belt of Dongying sag. Acta Pet. Sin. 42 (2), 163–175. https://doi.org/10.7623/syxb202102002 (in Chinese).

Lu, H., Niu, C.M., Li, H.Y., et al., 2020. Reservoir feature and evaluation of metamorphic buried-hill reservoir. Fault-Block Oil Gas Field 27 (1), 28–33. https://doi.org/10.6056/dkyqt202001006 (in Chinese).

Luo, G.M., Qi, S.W., Zheng, B.W., 2022. Rate effect on the direct shear behavior of granite rock bridges at low to subseismic shear rates. J. Geophys. Res. Solid Earth 127, e2022JB024348. https://doi.org/10.1029/2022JB024348.

Marcussen, Ø., Maast, T.E., Mondol, N.H., et al., 2010. Changes in physical properties of a reservoir sandstone as a function of burial depth——the Etive Formation,

northern North Sea. Mar. Petrol. Geol. 27 (8), 1725–1735. https://doi.org/10.1016/j.marpetgeo.2009.11.007.
Mclennan, S.M., 1993. Weathering and global denudation. J. Geol. 101 (2), 295–303. https://doi.org/10.1086/648222.
Nakata, Y., Hyodo, M., Hyde, A.F.L., et al., 2001. Microscopic particle crushing of sand subjected to high pressure one-dimensional compression. Soils Found. 41 (1), 69–82. https://doi.org/10.3208/sandf.41.69.
Nelson, R.A., Moldovanui, E.P., Matcek, C.C., et al., 2000. Production characteristics of the fractured reservoirs of the La Paz field, Maracaibo basin, Venezuela. AAPG Bull. 84 (11), 1791–1809. https://doi.org/10.1306/8626c393-173b-11d7-8645000102c1865d.
Nguen, H.B., Isaev, V.I., 2017. Oil reservoirs of the crystalline basement of the White Tiger field. Geofiz. Zh. Orig. 39 (6), 3–19. https://doi.org/10.24028/gzh.0203-3100.v39i6.2017.116363.
Nguyen, T.T.B., Satir, M., Siebel, W., et al., 2004. Granitoids in the Dalat zone, southern Vietnam: age constraints on magmatism and regional geological implications. Int. J. Earth Sci. 93 (3), 329–340. https://doi.org/10.1007/s00531-004-0387-6.
Niu, S.D., Guo, J., Xing, G.F., et al., 2022. In situ mineral chemistry of chlorite in Donghua area, Dehua-Youxi-Yongtai ore district, Fujian Province, south-east China: elemental characteristics and their implications for exploration. Geol. J. 57 (4), 1439–1455. https://doi.org/10.1002/gj.4349.
Novikov, V.M., Boeva, N.M., Bortnikov, N.S., et al., 2018. Chai Mat Kaolin–Bauxite deposit (South Vietnam): typomorphic features of kaolinite and formation mechanism of the zonal profile of the Bauxite-Bearing weathering crust of granites. Geol. Ore Deposits 60 (6), 513–526. https://doi.org/10.1134/s107570151806003x.
Riber, L., Dypvik, H., Sørlie, R., 2015. Altered basement rocks on the Utsira high and its surroundings, Norwegian North Sea. Norw. J. Geol. 95, 57–89. https://doi.org/10.17850/njg95-1-04.
Riber, L., Dypvik, H., Sørlie, R., et al., 2016. Clay minerals in deeply buried paleoregolith profiles, Norwegian North Sea. Clay Clay Miner. 64, 588–607. https://doi.org/10.1346/ccmn.2016.064036.
Riber, L., Dypvik, H., Sørlie, R., et al., 2017. Comparison of deeply buried paleoregolith profiles, Norwegian North Sea, with outcrops from southern Sweden and Georgia, USA—implications for petroleum exploration. Palaeogeogr. Palaeoclimatol. Palaeoecol. 471, 82–95. https://doi.org/10.1016/j.palaeo.2017.01.0430.
Riber, L., Driese, S.G., Stinchcomb, G.E., et al., 2019. Reconstructing a high paleolatitude Mesozoic paleoenvironment from a truncated and deeply buried regolith, Norwegian North Sea. Palaeogeogr. Palaeoclimatol. Palaeoecol. 528, 60–77. https://doi.org/10.1016/j.palaeo.2019.04.031.
Salah, M.G., Alsharhan, A.S., 1998. The Precambrian basement: a major reservoir in the rifted basin, Gulf of Suez. J. Pet. Sci. Eng. 19 (3–4), 201–222. https://doi.org/10.1016/s0920-4105(97)00024-7.
Shao, J.Q., Yang, S.Y., 2012. Does chemical index of alteration (CIA) reflect silicate weathering and monsoonal climate in the Changjiang River basin? Chin. Sci. Bull. 57 (11), 933–942. https://doi.org/10.1007/s11434-011-4954-5 (in Chinese).
Streckeisen, A., 1976. To each plutonic rock its proper name. Earth Sci. Rev. 12, 1–33. https://doi.org/10.1016/0012-8252(76)90052-0.
Wang, X., Zhou, X.H., Xu, G.S., et al., 2015. Characteristics and controlling factors of reservoirs in Penglai 9-1 large-scale oilfield in buried granite hills, Bohai Sea. Oil Gas Geol. 36 (2), 262–270. https://doi.org/10.11743/ogg20150211 (in Chinese).
Williams, J.J., 1972. Augila field, Libya: depositional environment and diagenesis of sedimentary reservoir and description of igneous reservoir: case histories. In: King, R.E. (Ed.), Stratigraphic Oil and Gas Fields-Classification, Exploration Methods, and Case Histories. AAPG Mem, pp. 623–632. https://doi.org/10.1306/m16371c48.
Xiao, F., Fan, F.P., Xing, G.F., et al., 2021. Ore genesis of Qingyunshan Cu-Au deposit in the Dehua-Youxi area of Fujian Province, southeastern China: constraints from U-Pb and Re-Os geochronology, fluid inclusions, and H-O-S-Pb isotope data. Ore Geol. Rev. 132, 104006. https://doi.org/10.1016/j.oregeorev.2021.104006.
Xu, C.G., Yu, H.B., Wang, J., et al., 2019. Formation conditions and accumulation characteristics of Bozhong 19-6 large condensate gas field in offshore Bohai Bay Basin. Petrol. Explor. Dev. 46 (1), 25–38. https://doi.org/10.1016/s1876-3804(19)30003-5 (in Chinese).
Xu, X.T., Shao, L.Y., 2018. Limiting factors in utilization of chemical index of alteration of mudstones to quantify the degree of weathering in provenance. J. Palaeogeogr. 20 (3), 515–522. https://doi.org/10.7605/gdlxb.2018.03.038 (in Chinese).
Xu, Y.X., He, W.P., Xu, L., et al., 2017. Analysis of lithospheric magnetic anomaly characteristics in Fujian region. China Earthquake Eng. J. 39 (6), 1084–1089. https://doi.org/10.3969/j.issn.1000-0844.2017.06.1084 (in Chinese).
Ye, T., Niu, C.M., Wei, A.J., 2020a. Characteristics and genetic mechanism of large granitic buried-hill reservoir, a case study from PengLai oil field of Bohai Bay Basin, north China. J. Pet. Sci. Eng. 189, 106988–107000. https://doi.org/10.1016/j.petrol.2020.106988.
Ye, T., Chen, A.Q., Niu, C.M., 2020b. Characteristics and vertical zonation of large-scale granitic reservoirs, a case study from Penglai oil field in the Bohai Bay Basin, North China. Geol. J. 55, 8109–8121. https://doi.org/10.1002/gj.3932.
Ye, T., Chen, A.Q., Niu, C.M., 2021. Structural, petrophysical and lithological characterization of crystalline bedrock buried hill reservoirs: a case study of the southern Jinzhou oilfield in offshore Bohai Bay Basin, north China. J. Pet. Sci. Eng. 196, 107950–107962. https://doi.org/10.1016/j.petrol.2020.107950.
Yu, Z.H., Lin, Y.B., Xiao, K.Y., et al., 2019. Characteristics and influence factors of basement buried-hill reservoir in Bongor Basin, Chad. Acta Petrol. Sin. 35 (4), 1279–1290. https://doi.org/10.18654/1000-0569/2019.04.20 (in Chinese).
Zhao, X.L., Yu, S.Y., Jiang, Y., et al., 2019. Petrogenesis of two stages of Cretaceous granites in south-west Fujian Province: implications for the tectonic transition of South-east China. Geol. J. 54 (1), 221–244. https://doi.org/10.1002/gj.3171.
Zhang, Y.Y., Wu, T., Gou, W., 2023. Reservoir characteristics and hydrocarbon accumulation models of the Bach Ho oilfield in Cuu Long Basin. Vietnam. Geol. Explor. 59 (1), 170–187. https://doi.org/10.12134/j.dzykt.2023.01.015 (in Chinese).
Zhou, X.M., Li, W.X., 2000. Origin of Late Mesozoic igneous rocks in Southeastern China: implications for lithosphere subduction and underplating of mafic magmas. Tectonophysics 326 (3–4), 269–287. https://doi.org/10.1016/S0040-1951(00)00120-7.
Zhu, M.L., Liu, Z., Liu, H.M., 2020. Structural division of granite weathering crusts and effective reservoir evaluation in the western segment of the northern belt of Dongying Sag, Bohai Bay Basin, NE China. Mar. Petrol. Geol. 121, 104612–104630. https://doi.org/10.1016/j.marpetgeo.2020.104612.
Zimmerman, R.W., Bodvarsson, G.S., 1996. Hydraulic conductivity of rock fractures. Transp. Porous Media 23 (1), 1–30. https://doi.org/10.1007/BF00145263.